



Deposited via The University of Sheffield.

White Rose Research Online URL for this paper:

<https://eprints.whiterose.ac.uk/id/eprint/126581/>

Version: Accepted Version

Article:

Bateman, M.D., Swift, D.A., Piotrowski, J.A. et al. (2018) Can glacial shearing of sediment reset the signal used for luminescence dating? *Geomorphology*, 306. pp. 90-101. ISSN: 0169-555X

<https://doi.org/10.1016/j.geomorph.2018.01.017>

Reuse

This article is distributed under the terms of the Creative Commons Attribution-NonCommercial-NoDerivs (CC BY-NC-ND) licence. This licence only allows you to download this work and share it with others as long as you credit the authors, but you can't change the article in any way or use it commercially. More information and the full terms of the licence here: <https://creativecommons.org/licenses/>

Takedown

If you consider content in White Rose Research Online to be in breach of UK law, please notify us by emailing eprints@whiterose.ac.uk including the URL of the record and the reason for the withdrawal request.

1 Can glacial shearing of sediment reset the signal used for luminescence dating?

2

3 Mark D. Bateman ^{a,*}, Darrel A. Swift ^a, Jan A. Piotrowski ^b, Edward, J. Rhodes ^a, Anders
4 Damsgaard ^{b,1}

5

6 ^a *Department of Geography, University of Sheffield, UK*

7 ^b *Department of Geoscience, Aarhus University, Denmark*

8 *now at Geophysical Fluid Dynamics Laboratory, NOAA / Princeton University, USA*

9

10 * Corresponding author. E-mail address: m.d.bateman@sheffield.ac.uk (M.D.Bateman).

11 ¹ Current address: Geophysical Fluid Dynamics Laboratory, NOAA / Princeton University, USA

12

13

14

15 **Abstract**

16 Understanding the geomorphology left by waxing and waning of former glaciers and ice sheets
17 during the late Quaternary has been the focus of much research. This has been hampered by the
18 difficulty in dating such features. Luminescence has the potential to be applied to glacial sediments
19 but requires signal resetting prior to burial in order to provide accurate ages. This paper explores the
20 possibility that, rather than relying on light to reset the luminescence signal, glacial processes
21 underneath ice might cause resetting. Experiments were conducted on a ring-shear machine set up
22 to replicate subglacial conditions and simulate the shearing that can occur within subglacial
23 sediments. Luminescence measurement at the single grain level indicates that a number (albeit
24 small) of zero-dosed grains were produced and that these increased in abundance with distance
25 travelled within the shearing zone. Observed changes in grain shape characteristics with increasing
26 shear distance indicates the presence of localised high pressure grain-to-grain stresses caused by

27 grain bridges. This appears to explain why some grains became zeroed whilst others retained their
28 palaeodose. Based on the observed experimental trend, it is thought that localised grain stress is a
29 viable luminescence resetting mechanism. As such relatively short shearing distances might be
30 sufficient to reset a small proportion of the luminescence signal within subglacial sediments. Dating
31 of previously avoided subglacial sediments may therefore be possible.

32

33 *Keywords:* glacial grinding; shear stress; luminescence

34

35

36 **1. Introduction**

37

38 As the Quaternary is typified by growth and decay of ice sheets and glaciers it is hardly
39 surprising that much research has focussed on using geomorphology to reconstruct and model these
40 through time (e.g., Jenson et al., 1995; Dyke et al., 2001; Clark et al., 2012; Toucane et al., 2015;
41 Hughes et al., 2016). Unfortunately, many of the difficulties and controversies stemming from this
42 can be traced back to uncertainties associated with age either through problematic stratigraphic
43 correlation or through methods attempting to provide specific ages (e.g., Hamblin et al., 2005; Pawley
44 et al., 2008; Gibbard et al., 2009; White et al., 2010, 2016; Lee et al., 2011). Radiocarbon is of
45 limited use as it covers only part of the last glacial-interglacial cycle, and organic preservation within
46 glacial sediments is limited and has a high potential for carbon recycling/contamination (Briant and
47 Bateman, 2009). Uranium series dating and amino-acid racemisation often cannot be applied through
48 lack of suitable material within glacial sequences. As a result, Quaternary scientists largely apply
49 cosmogenic and luminescence dating. The application of cosmogenic exposure dating, although
50 relatively new, has been making a significant contribution to the understanding of ice-sheet

51 fluctuations (e.g., McCormack et al., 2011; Anjar et al., 2014; Davis et al., 2015). However, exposure
52 dating is largely limited to glacially eroded boulders on, for example, moraines and crag-and-tails
53 (e.g., Livingstone et al., 2015a) and is complicated by the presence of cold-based ice (Ballantyne,
54 2010).

55 Luminescence dating has potential to date events within the last two glacial-interglacial cycles
56 (e.g., Bateman et al., 2011) and is applicable to quartz and feldspars that are almost ubiquitous within
57 preserved glacial landforms and sediments. As such, the method is attractive for gaining glacial
58 chronological frameworks. However, the technique relies on the fundamental premise that at some
59 point between erosion, transport, or deposition, glacial sediment must be exposed to sunlight for a
60 sufficient duration to remove antecedent stored luminescence. Godfrey-Smith et al. (1988) showed
61 that for quartz the optically stimulated luminescence (OSL) signal is reduced to <1% of its original
62 level within 10 seconds of sunlight exposure. It therefore might be viewed that this is not too hard a
63 criterion to meet, and indeed, King et al. (2014a, 2014b) showed that sediment redistribution in
64 proglacial settings has a number of opportunities to reset. However, many of the events/sediment
65 requiring dating pertain to subglacial processes and associated landforms in which light exposure is
66 unlikely (e.g., Lamothe, 1987; Rhodes and Pownall, 1994; Fuchs and Owen, 2008). As a result, age
67 overestimation (e.g., Duller et al., 1995; Houmark-Nielsen, 2009) and ages in saturation or highly
68 variable ages (e.g., Thrasher et al., 2009) can occur.

69 It has long been established that electrons trapped in defects within the crystal lattice of quartz or
70 feldspar can also be stimulated into releasing luminescence by heat (thermoluminescence or TL) from
71 natural or anthropogenic fires. What is less well established is a third environmental luminescence
72 stimulation mechanism that relies on frictional effects or pressure (McKeever, 1985), which is known
73 to cause triboluminescence or piezoluminescence. In this, as electrons recombine and give off
74 luminescence, so the stored charge depletes, eventually leading to resetting (see Dreimanis et al.,

75 1978; Aitken, 1985; Lamothe, 1988; Toyoda et al., 2000). Studies of sediment found in deep faults
76 have shown that luminescence resetting does occur during earthquake events, but in such cases the
77 ambient temperature is elevated and pressures induced by overburden as well as during movement on
78 the fault are high (Zöller et al., 2009; Spencer et al., 2012). Subglacial temperatures and general
79 confining pressures are much lower than this. Nonetheless, the existence of resetting at the ice-bed
80 has been proposed (e.g., Morozov, 1968; Dreimanis et al., 1978; Lamothe, 1988). More recently,
81 empirical work from the Haut Glacier d’Arolla, Switzerland, by Swift et al. (2011) appeared to
82 show a lowered luminescence signal from subglacial samples when compared to supraglacial
83 sediments. This they suggested was caused by the resetting of sediment during subglacial crushing
84 and grinding (specifically, bedrock erosion and debris comminution).

85 Laboratory studies of the effects of mechanical crushing on sediment luminescence have
86 generally failed to see an effect (e.g., Sohbati et al., 2011; Rittenour et al., 2012). However,
87 Bateman et al. (2012) reported initial results from a ring-shear experiment in which changes to
88 palaeodose (D_e) were monitored as shearing distance increased. This demonstrated for the first time
89 that changes in stored palaeodose are possible when sediment was placed under a modest pressure
90 (100 kPa) and sheared. They suggested that the average confining pressure applied within the ring-
91 shear apparatus was insufficient alone to cause these changes. Instead, they concluded that stress
92 induced during grain bridging (grain stacks or forced chains consisting of several aligned grains)
93 events was important. They therefore suggested that geomechanical luminescence signal reduction
94 may be a viable alternative mechanism for resetting (referred to as ‘bleaching’ when performed by
95 light) of glacial sediments. However, the experiment on its own was not conclusive as it was
96 hampered by low quantities of grains showing signs of resetting and high levels of palaeodose
97 scatter. It was also impossible to discern, because of the low palaeodose (~4 Gy) of the sediment
98 used, whether grains were being fully reset or their stored dose just depleted. Finally, the

99 experiment was unable conclusively proved whether the observed changes in palaeodose were
100 caused by pressure (normal stress), shear stress, or other mechanical changes such as localised
101 recrystallization (or the causation and migration of defects within grains).

102 The aims of this present study were twofold. First, to test the results of Bateman et al. (2012)
103 using an annealed gamma irradiated sample with much higher dose, increased sensitivity, and lower
104 initial D_e scatter. It was hoped such an approach would provide the opportunity to see more
105 effectively whether OSL signal resetting is actually taking place or just that palaeodose is being
106 reduced. Second, using new surface texture and shape data from the Bateman et al. (2012)
107 experiment and the new experiment to better understand the potential mechanisms causing any
108 signal removal.

109

110 **2. Experimental details**

111

112 *2.1. Sample preparation*

113

114 The experiment of Bateman et al. (2012; experiment 1) and the new experiment (experiment 2)
115 were based on sediment sampled from a dune field at Lodbjerg, Denmark, studied by Murray and
116 Clemmensen (2001) and Clemmensen et al. (2009). This sediment was originally derived from
117 local, sand-rich glacial till. Actual glacial sediment was not used because of its complex transport
118 history (e.g., Fuchs and Owen, 2008), sometimes poor OSL sensitivity (e.g., Preusser et al., 2007),
119 and mixed lithologies that may be associated with different luminescence properties and behaviour
120 (Rhodes and Bailey, 1997; Rhodes, 2000). Sampling consisted of driving 50+ opaque 20-cm-
121 diameter PVC tubes into the exposed dune face (Fig. S1). The tubes were transported to the
122 laboratory, where the outer 2–3 cm of sand from each tube-end was discarded (thus excluding any

123 grains that may have been exposed to light). Sand was then sieved through a 500 μm sieve to
124 remove extraneous organic material (mostly small rootlets) and homogenised by mixing.
125 Mineralogy was confirmed to be dominantly quartz by mineral-mapping ~ 100 grains using a Zeiss
126 Sigma field emission analytical SEM equipped with an Oxford Instruments INCAWave detector.
127 Further, laser granulometry confirmed the size distribution to be well-sorted medium sand ($M_d =$
128 $295 \mu\text{m}$, $d_{10} = 197 \mu\text{m}$, $d_{50} = 319 \mu\text{m}$, $d_{90} = 543 \mu\text{m}$).

129 For the new experiment (experiment 2), sediment was additionally annealed to 500°C for 1
130 hour to remove any naturally acquired palaeodose and to improve the quartz sensitivity to dose.
131 The sediment was then given a 38.1 ± 1.2 Gy dose using the Cobalt⁶⁰ gamma source at Risø,
132 Denmark. This dose was selected to be of a similar magnitude to what would be expected for a
133 relict glacial deposit from the Last Glacial Maximum (~ 21 ka). As the annealing and gamma dosing
134 was undertaken in batches, all were thoroughly remixed prior to ring-shear experimentation.

135

136 2.2. *Shearing in the ring-shear*

137

138 For both experiments, sediment was loaded under dark room conditions into the Aarhus
139 University ring-shear apparatus (Fig. 1A). The ring-shear consists of a large (sample surface of
140 1800 cm^2) circular shearing chamber with a trough for the sediment 120 mm wide and depth of 80
141 mm (see Larsen et al., 2006, for further details). It has two plates between which the shearing gap in
142 the sample is located. Ribs 6 mm in length are attached to both plates to fix the sample, and
143 shearing is created by rotating the lower plate at a constant velocity (Fig. 1B). A uniform normal
144 stress is applied hydraulically to the sample through the normal-load plate, which is free to move
145 vertically according to sample compaction or expansion during shearing. Shear stress is measured
146 by two sensors mounted on the normal-load plate, and sediment compaction is monitored by three

147 sensors attached to the normal-load plate at equal distances around the shearing chamber whereby
148 average data recorded by each group of sensors are considered further. The approximate shearing
149 zone position was determined during test runs conducted using glass beads as strain markers, which
150 showed the zone of deformation to be around 2.5 cm thick (Fig. S3). During the shearing, the sand
151 had a preexisting moisture content making it cohesive but not saturated.

152 For experiment 1, the ring shear apparatus was run at a uniform normal stress of 100 kPa and a
153 shearing velocity of 1 mm min^{-1} (i.e. parameters that are in the range of typical conditions beneath
154 glaciers and ice sheets; Paterson, 1994) to a distance of 1280 cm. During the experiment, sediment
155 compaction, shear stress, and normal stress were recorded in 30 second intervals. Experiment 1 was
156 periodically paused to allow sampling after shearing displacements of 10, 20, 40, 80, 160, 320, 640,
157 and 1280 cm. At each pause, two opaque 20-mm-diameter tubes were inserted vertically into the
158 sand in the middle of the shearing chamber, marked at the level of the shearing chamber sand, and
159 then slowly pulled out and sealed. The mark was subsequently used to infer the location of the
160 shearing zone in each sample. The space in the shearing chamber left after sampling was naturally
161 backfilled by lateral sediment creep while the tube was removed so that the original stratification
162 was reinstated as closely as possible. This formed the basis of the samples used for sediment and for
163 OSL characterisation. Before the start of the shearing and after each sampling, the sediment was
164 consolidated under the normal stress of 100 kPa. Experiment 2 was run with the same parameters as
165 above except that after shearing displacement of 1280 cm, normal stress was increased to 150 kPa
166 and velocity to 2 mm min^{-1} and a final sample was collected after a total shearing displacement of
167 1920 cm.

168
169 **[Fig. 1 here]**
170

171 2.3. Luminescence measurements

172

173 All OSL sample preparation and analyses of samples from experiment 2 were carried out in the
174 University of Sheffield luminescence laboratory under controlled lighting conditions. For each
175 ring-shear sample, subsamples were taken by cutting 1-cm sections of tube with a pipe-cutting tool.
176 This avoided any mechanical damage to grains that sawing would have caused. The position of the
177 shearing zone was determined based on a prior test experiment using glass beads as strain markers
178 that showed a 2.5-cm-thick shearing zone located in the middle of the sample tube (see
179 supplementary information for more details). Two sets of subsamples were collected: (i) from 1 cm
180 below the shearing zone (referred to herein as unsheared), and (ii) centred on the shearing zone
181 (referred to herein as sheared). The former samples were taken for the purpose of investigating the
182 effects of pressure alone and the latter for the combined effects of shear stress and pressure.

183 The OSL measurements focussed on quartz rather than feldspar as quartz dominated in terms
184 of grain numbers within these small samples and feldspar grains have potential anomalous fading
185 issues. The quartz from all subsamples was extracted and cleaned for OSL dating (see Bateman and
186 Catt, 1996, for details). Given the limited sample size, prepared quartz between 90 and 250 μm
187 diameter was used. Single grain OSL measurements were made on a TL-DA-15 Risø reader with a
188 green laser single grain attachment (Duller et al., 1999). In principle, with the grain size used, more
189 than one grain could have been mounted in the 300 μm Risø grain holder and measured
190 simultaneously. However, given that <10% of grains were smaller than 197 μm and that most
191 grains emitted insufficient OSL, the chances of more than one grain contributing to a stored dose
192 (D_e) was considered extremely low. Luminescence was filtered with a 2.5-mm-thick Hoya U-340
193 filter (as per Ballarini et al., 2005) and irradiation was provided by a calibrated $^{90}\text{Sr}/^{90}\text{Y}$ beta source.
194 The OSL stimulation was for 0.8-s, whilst the sample was held at 125°C. The D_e values within

195 grains were measured using a single aliquot regeneration (SAR) protocol with a 10-s, 260°C preheat
196 experimentally determined from a dose recovery preheat plateau test (Murray and Wintle, 2003).
197 The SAR growth curves for each grain were based on an integral of OSL measured between 0.08
198 and 0.11 s and background on an integral of OSL measured between 0.64 and 0.8 s. When
199 analysing the SAR data, grains were only accepted where the recycling ratio was 1 ± 0.2 of unity;
200 recuperation was <5%; the error on the test dose was <20%; the naturally acquired OSL was
201 significantly above background; and SAR regeneration points could be fitted by a growth curve. To
202 demonstrate the appropriateness of this measurement protocol, dose recovery tests were undertaken
203 with two samples (Shfd12089 and Shfd12090), which both returned measured palaeodoses within
204 unity of those given (1.03 ± 0.03 and 1.02 ± 0.03 respectively), low overdispersion (7% and 5%),
205 and normal D_e distributions (Fig. S5). Importantly, given the subsequent results from the ring-shear
206 experiment samples, no zero-dose grains were measured during these dose recovery tests.

207

208 [Table 1 here]

209 The natural sediment used in Bateman et al. (2012) required 3000-5000 grains to be measured
210 per sample to meet a minimum of 35 accepted grains. Annealing clearly improved the sediment
211 sensitivity as only between 400 and 1300 grains per sample needed to be measured for a minimum
212 of 50 D_e values to meet the acceptance criteria (Rodnight, 2008). Data shown in Tables 1 and 2
213 represent the measurement of over 21,000 grains. As it was key to find potentially small numbers
214 of reset (i.e. zero-dose) grains and grains with depleted D_e values, two subsamples (see samples
215 Shfd12089 and Shfd12090 in Table 1) were measured independently three times to evaluate the
216 reproducibility of results. For the purposes of this experiment, zero-dose grains were defined as
217 those with D_e values within uncertainty of 0 Gy and their numbers were recorded as a percentage of
218 the accepted grains. Results were analysed using the central age model (CAM; Galbriath et al.,
219 1999), which also allowed calculation of overdispersion (OD; percentage of uncertainty greater than
220 can be explained by the errors calculated around the central value). As the data sets were non-
221 normally distributed results were also analysed with the finite mixture model (FMM; Galbraith and
222 Green 1990) where a σb value of 0.20 was used (as per Livingstone et al., 2015b) and k was
223 selected to minimize the Bayesian information criterion (BIC) value.

224

225 [Table 2 here]

226

227 2.4. Sediment characterisation measurements

228

229 Changes in grain shape were quantified at first manually (experiment 1) and then using
230 automated image-based methods (experiments 1 and 2). Manual analysis was performed by visual
231 classification of grains viewed under a microscope using Power's roundness index (Powers, 1953).
232 Automated analysis was used to measure specific grain attributes (including particle area, perimeter

233 length, Feret, and breadth) that enable calculation of common shape parameters (Table 3). First,
234 optical or SEM images of 50 randomly selected grains per subsample were analysed using the
235 ‘Gold Morph’ shape-analysis plug-in (Crawford and Mortensen, 2009) for the ImageJ image
236 processing and analysis software programme (imagej.nih.gov/ij/). Second, the remaining material
237 was analysed using a Sympatec QICPIC Image Analyser system fitted with a 532-nm laser and a
238 high-speed (70 Hz s^{-1}) CMOS camera, which permitted analysis of 19,000+ particles per sample.

239 Calculated shape parameters are shown in Tables 3 and 4 (parameter variables are defined in
240 Table 5). Parameters for optical and SEM image analysis (Table 3) were selected for their
241 sensitivity to changes in grain shape as illustrated by the accompanying diagrams to Krumbein’s
242 (1941) scale of roundness (shown in modified form in Figure S2). Parameters in Table 4 are
243 calculated automatically by the QICPIC analysis software. Two of these (*Sphericity* and *Convexity*)
244 have direct equivalents in Table 3 (although their outputs are inverted), whilst *Aspect Ratio* has
245 some equivalency to *Round* (Table 3) because these parameters relate either longest or shortest
246 length to particle area. All such parameters are limited in that they allow characterisation of overall
247 particle form only, whereas the Krumbein and Power’s Roundness indexes require the user to
248 classify particles based on a combination of overall form (e.g., their *blockyness*) and individual edge
249 characteristics (e.g., the ‘sharpness’ of their asperities). However, because edge characteristics
250 (including fractures) do contribute to overall form of small particles, these more quantitative
251 approaches should offer significant advantages over manual (e.g., Power’s) techniques. The
252 QICPIC parameters are by default calculated for grains in specific size ranges, meaning, for
253 simplicity, individual size-category values were combined into a single mean value.

254 In addition to the above, at the end of experiment 1 a vertical thin section oriented parallel to
255 the shearing direction along the middle of the sample was prepared from an undisturbed sediment
256 block. This was to permit examination of grain arrangement and characteristics *in situ* (i.e. within

257 the shearing zone). The thin section was subdivided into 18 equally thick segments and in each of
258 them, the orientation of elongated grains was determined separately. On average, 32 grains with
259 axial ratios of at least 2:1 per segment were measured. The orientations are expressed as S_1
260 eigenvalues (Mark, 1973) and as main dip angles (MDA) representing the averaged angle of dip of
261 the 18°-wide sector of rose diagram that contains the highest number of single measurements.

262

263 **3. Results**

264

265 *3.1. Luminescence*

266

267 Luminescence results for experiment 1 were presented in Bateman et al. (2012) so only the new
268 results for experiment 2 are outlined here. For the unsheared subsamples, with progressive shearing
269 the mean D_e (based on CAM) shows a slight decrease after 80 cm, but with an r^2 of only 0.02 this is
270 not significant (Fig. 2A). For sheared samples, the mean D_e shows a slight decrease after 320 cm,
271 but with an r^2 of only 0.08 again this is not significant especially if the final point is excluded on the
272 basis that it was sheared at a high normal stress (150 not 100 kPa; Fig. 2B). All samples showed a
273 surprising level of OD that was on average 30% (Table 1) and did not increase with shearing
274 distance. Looking at the FMM results, both sets of subsamples show weak trends towards
275 decreasing D_e with shearing distance (Fig. 3). The r^2 values are higher than the CAM (0.2 and 0.4
276 respectively) reflecting FMM isolating some small (<10% of the data) components for some
277 samples. The latter may reflect a small number of measurements where more than one grain was
278 measured simultaneously. Zero-dose values through necessity had to be excluded from the
279 logarithm-based FMM analysis.

280 More than one FMM component was found with some sheared and unsheared subsamples, but
281 this is not a systematic effect. To check this, two randomly selected samples were run
282 independently three times to establish internal variability in the mean and component D_e values
283 (Table 2). Sample Shfd15090 returned CAM D_e values within errors but one replicate had only one
284 FMM component compared to the two components of the other two replicates. For sample
285 Shfd15089, one replicate returned two FMM components compared to the one component
286 identified for the other two replicates. Additionally, one of the replicates failed to return a CAM D_e
287 within errors of the other two replicates. In the light of the variability of the replicate data, and
288 despite using a σb value three times higher than the OD established with the dose recovery
289 experiments (5-7% measured, 20% applied) and minimising the BIC, FMM failed to accurately fit
290 to and extract components from these data, and the results are therefore unreliable.

291

292 **[Figure 2 here]**

293

294 **[Figure 3 here]**

295 The critical luminescence data appear to be the number of zero-dose grains measured. No
296 zero-grains were found in the 10 samples (>10,000 grains measured) taken from the unsheared zone
297 regardless of the shearing distance travelled. Further, no zero-grains were measured on the sheared
298 material during the two dose-recovery experiments undertaken (1600 grains measured, Figure S5).
299 Zero-grains appeared only within the shearing zone after the shearing distance exceeded 100 cm
300 (after 2400 grains from shorter distances had already been measured). As shown in Fig. 4, as a
301 function of total grains that met the quality acceptance criteria, zero-dose grains remained low
302 (max. 8 grains out of 80 grains in sample Shfd12095) but linearly increased with shear distance (r^2
303 = 0.8; note logarithmic distance scale in Fig. 4). Whilst the number of zero-dose grains was small,
304 this is the second separate experiment that has generated them (the first being that of Bateman et al.,
305 2012). Further measurements for longer distances could not be undertaken because of constraints
306 on machine time (ring-shear experiment 2 took over 13 days to run excluding stops to permit
307 sampling) and because at longer distances multiple rotations of the circular ring-shear machine
308 increased the possibility of collecting sediment already disturbed by earlier sampling.

309

310 [Figure 4 here]

311

312 3.2. Sediment characterisation

313 Results demonstrated that, despite an initial degree of angularity and fracture presence, experiment
314 1 sheared zone subsamples exhibited increasing angularity and elongation with shearing distance
315 (e.g., Fig. 5, Table 6), confirmed by Power's roundness and fracture incidence (Table 7). Most
316 notably, analysis of SEM grain images demonstrated observable correlation with shearing distance
317 (here defined as $p \leq 0.1$) for parameters *Conv2* and *Round*, weakly observable correlations ($p \leq$
318 0.35) for parameters *rP* and *Conv*, and a significant correlation ($p \leq 0.05$) for the parameter *Circ*

319 (Figs. 5 and 6; Table 6). This was supported by QICPIC analysis, which demonstrated a significant
320 correlation with shearing distance ($p \leq 0.05$) for *Convexity* (Table 6). Interestingly, QICPIC size
321 results (Table 5) also demonstrated a statistically significant correlation between particle size and
322 shearing distance, demonstrating an increase in sediment size within the shearing zone.

323 Experiment 2 shearing zone subsamples are not entirely consistent with those for experiment
324 1, demonstrating some inconsistent parameter changes, including a decrease in the *Circ* parameter
325 and particle diameter, an increase in the *Conv2* and *Sphericity* parameters, and no apparent decrease
326 in the *Conv* and *Round* parameters (Table 6). Some parameter changes consistent with experiment 1
327 were instead observed in unsheared subsamples, specifically for *Circ*, *Conv*, *Round*, *Convexity*, and
328 *Aspect Ratio*, together with a weakly observable increase in particle size (Table 6); although
329 *Sphericity* was again observed to increase. Manual analysis did nonetheless demonstrate some
330 change in Power's roundness and fracture incidence for sheared zone subsamples and failed to
331 show any observable changes for unsheared samples (Table 7). These less clear-cut results for
332 experiment 2 appear to indicate that the shearing zone constituted a wider, more diffuse zone than
333 observed during experiment 1.

334

335 [Figure 5 here]

336 [Figure 6 here]

337

338 [Tables 6 and 7 here]

339

340 [Figure 7 here]

341

342

343 Thin section results from experiment 1 demonstrated that S_1 values, which express the
344 orientation strength of elongated grains, were between ~ 0.42 and ~ 0.76 and grains typically

345 exhibited low-angle dips (Figs. 8 and 9). There was no clear pattern in the orientation strength
346 within the shearing chamber, but two peaks are visible (Fig. 8). The peak of S_1 values in the middle
347 of the shearing zone is attributed to grain advection and rotation toward quasi-stable positions with
348 grain long axes oriented parallel to the shearing direction (Hooyer et al., 2008). The second peak at
349 the top of the deposit, well above the shearing zone, is possibly caused by repeated compaction that
350 the deposit has been subjected to at the start of each shearing increment. There is no systematic
351 downflow or upflow dip direction of elongated grains within the shearing zone.

352

353 [Figure 8 here]

354 [Figure 9 here]

355

356 *3.2. Ring shear monitoring data*

357

358 Parameters recorded during experiment 2 are shown in Fig. 10. During this experiment, the
359 prescribed normal stress (100 or 150 kPa) varied by $\leq \pm 0.12$ kPa, which is negligible. The total
360 compaction of the sediment at the end of experiment reached about 6 mm reflecting a combination
361 of pore space reduction because of denser grain packing and grain-size reduction due to grain
362 abrasion and fracturing. However, some apparent compaction also occurred as a result of sediment
363 being squeezed out of the chamber through the shearing gap (although not measurable the volume
364 was estimated as $< 1\%$ in relation to the overall sediment volume in the chamber). The highest
365 compaction rates were achieved at the beginning of the shearing whereby half of the total
366 compaction (~ 3 mm) occurred during the initial shearing displacement of ~ 5 cm. After about 170
367 cm of shearing, compaction became approximately linear and small and increased slightly again
368 during the last shearing increment under increased normal stress of 150 kPa. Despite the granular
369 character of the material, no dilatant volume increase at the beginning of shearing was noticed,

370 possibly because of the fine-grained nature of the sand. The average shear stress generated in the
371 deforming material was ~36 kPa during the shearing under normal stress of 100 kPa and ~55 kPa
372 under normal stress of 150 kPa. During the entirety of experiment 2, shear stresses fluctuated
373 significantly with an amplitude of up to ~18 kPa. Stress variations of several kPa occurred over
374 shearing displacements of just a few centimetres (Fig. 10). After a shearing displacement of about
375 800 cm certain cyclicity in stress fluctuations with a wavelength of around 60 cm became apparent.
376 This was possibly caused by recurrent grain-rearrangement events that become predictable after a
377 quasi-steady state of deformation has been reached. During shearing under normal stress of 100
378 kPa, the magnitude of stress variations increased toward the end of the experiment and remained
379 high during shearing under normal stress of 150 kPa.

380

381 [Figure 10 here]

382

383 **4. Discussion**

384

385 The marker displacement of shearing chamber sediments reported in Bateman et al. (2012)
386 indicated that shearing took place within a narrow, well-defined shearing zone. This is supported by
387 sediment characterisation of the sheared subsamples from experiment 1 that indicated the evolution
388 of particle shape toward more angular and elongated morphologies. This is consistent with
389 fracturing of grain surfaces as a result of grain-grain stresses imposed during sediment deformation
390 and an increase in apparent average grain size. Thin section results also indicate the development of
391 alignment of larger grains in the shearing zone. It is proposed that the apparent grain size increase
392 and alignment observations result from the rotation of larger grain in the shearing zone causing

393 smaller grains to be expelled from it. As a result of the cohesive nature of the sediment and lack of
394 free-water, it is possible that grains were expelled in both directions.

395 Mixed observations of size and shape changes for both sheared and unsheared subsamples from
396 experiment 2 indicate that the shearing zone may have occurred in a wider zone than for experiment
397 1. It may be possible to disregard the inconsistent *Circ*, *Conv2*, and *Sphericity* parameter changes
398 observed for sheared zone samples. *Circ* and *Sphericity* (Tables 3 and 4) relate particle perimeter
399 length to that of an idealised sphere of the same area, which is unlikely to apply to initially
400 nonspherical geological particles. *Conv2* (Table 3) uses perimeter length to calculate convexity and
401 is therefore likely to capture changes in surface roughness rather than overall form. However, the
402 statistically significant decrease in grain size shown by the sheared samples, which is inconsistent
403 with experiment 1, remains. Irrespective of this, grains in the sheared and unsheared subsamples
404 might be expected to have experienced high stresses and mechanical fracture.

405 Based on the luminescence results in this current experiment we can confirm some of the
406 preliminary findings reported in Bateman et al. (2012). In the latter, they reported that shearing led
407 to changes in D_e distributions with grains displaying increases and decreases in D_e including some
408 zero-dosed grains. It was hoped that in experiment 2, with a much higher stored dose, with shearing
409 distance there would be more grains with a reduced (but not zeroed) D_e relative to the given dose.
410 This was not observed because, whilst sheared and unsheared subsamples returned individual grain
411 D_e values higher and lower than the given gamma dose, neither sets showed significant trend with
412 distance sheared. Experiment 2 did nonetheless confirm the increase in zero-dose grains observed
413 by Bateman et al. (2012, their Fig. 4) with the occurrence of a small number of zero-dose grains
414 increasing with shearing distance but only for sheared sediment grains. Taken together it would
415 appear that grains apparently have a bimodal response, either completely retaining their dose or
416 completely losing it during shearing.

417 This leads to the question as to what within the shearing process could be the cause of a
418 minority of grains to be reset whilst other grains are unaffected. Possible mechanisms include grain
419 fracture, which is postulated to reduce the number of active luminescence centres that are
420 surrounded by an extended atomic lattice (Toyoda et al., 2000), the ejection of trapped electrons by
421 stresses imposed on the crystal lattice (Lee and Schwarz, 1994), localised frictional heating at grain
422 boundaries (Fukuchi, 1989; Lee and Schwarz, 1994), and wear of grain surfaces leading to loss of
423 alpha-induced luminescence stored near grain surfaces (Lamothe, 1988; Takeuchi et al., 2006). The
424 results of this study indicate that grain fracture is unlikely because grain size observations appear to
425 support smaller grains being expelled from the shearing zone rather than this zone comprising
426 particles that have been cleaved. Further, sand-sized quartz grains formed by the comminution of
427 larger clasts beneath glaciers are thought to be highly resistant to further fracture (Wright, 1995),
428 indicating that observations of changes in grain size may result largely from sorting, as opposed to
429 cleavage. This is supported by observed grain shape changes being relatively modest, with
430 fracturing acting only to modify grain faces and edges.

431 Frictional heating at grain boundaries or wear to grain surfaces (e.g., Lamothe, 1988) is easily
432 excluded mainly because it would be localised at grain surfaces, such that any effect on
433 luminescence will have been removed by the HF acid etching during sample preparation.
434 Additionally, the use of a laser to stimulate grains during OSL measurement should ensure rapid
435 depletion of all optical traps throughout translucent quartz grains. If heterogeneity existed in trap
436 defects within the crystal lattice and only traps *near* the grain surface (but sufficiently deep they
437 survive etching) were storing dose, then the mechanical surface removal observed could potentially
438 lead to resetting. However, two arguments can be put forward against this. Firstly, mechanical
439 alteration appears to be related to shearing distance and so the amount of surface removed from a
440 grain could be expected to increase with distance. That being the case, we would expect to see a

441 rapid initial reduction in grain D_e as a result of the *high dose* grain surface being removed first, then
442 a slower reduction associated with the exposure of the *low dose* core. The OSL data from both
443 experiments do not detect initial D_e reduction only an increase in zero-doses. Secondly, some
444 mechanical alteration (Table 5) is also detected in the below shearing zone subsamples, for which
445 no zero-dose grains were observed. Thus, the reduction to zero-doses measured in experiments 1
446 and 2 could not just be occurring at grain surfaces, and the removal of some grain surfaces during
447 shearing apparently is not removing palaeodose for most grains.

448 Application of stress, on the other hand, might affect defects in the crystal lattice such that
449 localised recombination of electrons could occur giving rise to triboluminescence (Lee and
450 Schwarz, 1994) and lowering the overall dose within a grain. As the concentration of trapped
451 charge and the number of photons produced are low, this would seem unlikely. Alternatively,
452 elevated stress on the crystal lattice (and possibly associated temperature from friction; Fukuchi,
453 1989; Lee and Schwarz, 1994) could cause the redistribution of trapped charge into more unstable
454 traps thereby leading to apparent resetting when samples were measured months later. Simple
455 laboratory grinding of sediment with a pestle and mortar has been observed to reduce and increase
456 measured D_e through charge redistribution and/or triboluminescence (Phil Toms, Gloucester
457 University, pers. com.). Charge redistribution is supported by Bateman et al. (2012) who observed a
458 decrease with shearing of the stable 375°C TL peak with a corresponding increase in signal in the
459 less stable 240°C peak. Nonetheless, establishing this as a mechanism requires further work. For
460 example, it would be necessary to investigate the effect on the signal caused by the orientation of
461 the crystal structure relative to the maximum stress imposed by grain bridges.

462 It is clear in comparing the sheared and unsheared subsample sets that alterations to palaeodose
463 are not occurring simply as a result of general pressure (i.e. the normal stress) exerted on the
464 sediments (100 kPa). Had this been the case, zero-dosed grains would have been observed from

465 unsheared samples. Apparent resetting of the whole grain is concordant with elevated stresses
466 (over and above the pressure applied to all sediment) imposed on grain crystal lattices during
467 shearing. Shear stresses and the resulting strain distribution in granular materials are well known to
468 be highly heterogeneous (e.g., Drescher and de Josselin de Jong, 1972; Iverson et al., 1996; Li and
469 Aydin, 2010) and that the deforming material develops domains of different mechanical behaviour
470 with sizes across several orders of magnitude between millimetres (micromorphology) and
471 kilometres (macroelectronics) (Mandl et al., 1977). Experimental laboratory work has demonstrated
472 that uneven strain distribution results in the formation of discrete shear planes that focus sediment
473 advection whereas grains between the shear planes either remain largely stable or undergo
474 rotational movement (cf. Damsgaard et al., 2013) leading to sediment ‘skeleton’ evolution (e.g.,
475 Larsen et al., 2006, 2007; Narloch et al., 2012, 2015; Menzies et al., 2013). The latter may generate
476 grain bridges that support stresses up to several times (Iverson et al., 1996) or even an order of
477 magnitude (Mandl et al., 1977) greater than the general stress in the surrounding material. Grain
478 bridges fail by fracture of the particles, slip between the particles in the bridge, frictional slip
479 between the outermost particles in the bridge and the surface of blocks sliding above and below,
480 and by wear (abrasion) of the particles (Biegel et al., 1989; Hooke and Iverson 1995), all resulting
481 in spontaneous rearrangements of the skeleton and stress relief.

482 As stated earlier, strong evidence exists of pronounced stress heterogeneity during shearing
483 experiment 2, especially in its second half, when normal pressure was 150 kPa and induced shear
484 stress varied from 47 up to 65 kPa. Notably, these recorded stress values are an average value
485 resulting from multiple local stress events in the sample, and therefore the amplitude of grain-to-
486 grain stresses at the scale of grain bridges and local shear planes must have been significantly
487 greater. Brittle deformation of quartz grains has been observed at 200 Mpa (Bisshop et al., 2005)
488 and 7000 kPa with a strain rate around 10^{-12} s^{-1} (Gueydan et al., 2005). It is unlikely these sorts of

489 pressures occurred at the grain-to-grain level. However, if the work of Mandl et al. (1977) is
490 correct, pressures within bridges could have reached up to 650 kPa whilst others have suggested it
491 could exceed 5000 kPa (Boulton, 1974; Cohen et al., 2005). As grains move from spheroids to more
492 angular forms, as shown by the sediment data, so the potential for more uneven grain packing
493 leading to more frequent bridge-building events and more extreme stresses during these events
494 should increase. The increase in zero-dose grains with distance should therefore mirror changes in
495 grain shape and more variability in monitored stress data, which it does. Thus, some more angular
496 grains within highly stressed bridges could have had their D_e depleted, whereas other grains could
497 have avoided this by being located in more sheltered areas between the shear planes and grain
498 bridges. The net effect of this is the uneven yet distinct increase in numbers of zero-dose grains in
499 the shearing zone with increasing shearing displacement (Fig. 4).

500 Zero-dose grains have been measured from nonglacial environments. Some can be attributed to
501 post-depositional disturbance leading to grains moving to the surface, being reset and then being
502 reburied (e.g., Bateman et al., 2003, 2007). This is clearly not the case for this experiment or for
503 most glacial landforms. Other causes of zero-dose grains may be attributable to poor quartz
504 characteristics (e.g., Preusser et al., 2007), which has hampered dating of glacial sediment (e.g., in
505 the Swiss Alps) or measurement issues. The experiment presented here demonstrates that
506 measurement issues or sediment characteristics cannot account for the zero-dose grains measured. If
507 pressure across bridges between grains is the key resetting mechanism for subglacial sediments and
508 landforms then such conditions do not apply to other nonglacial environments. As such, findings
509 from this work cannot be directly extended to non-glacial environments except for sediments in
510 tectonic areas with active near-surface faults.

511 The observed increasing numbers of zero-dosed grains with shearing distance supports the
512 original findings of Swift et al. (2011) that the lower measured luminescence signals of sediment

513 sampled directly from the glacier bed beneath ~100 m of glacier at Haut Glacier d’Arolla,
514 Switzerland, were attributable had been reset. As many glacial sediments will have been in the
515 shearing zone for distance greatly exceeding that of this ring-shearing experiment, reset grains in
516 many glacial diamicts and landforms may be more prevalent than previously thought. This may
517 account for the relatively good resetting of sediment associated with glacial landforms that have
518 been obtained as part of the BRITICE-CHRONO project (e.g., Evans et al., 2017; Smedley et al.,
519 2017; Bateman et al., 2018). That many glacial studies have struggled in this regard may be more
520 because of insensitive quartz and poor intrinsic OSL characteristics of local bedrocks (e.g.,
521 Sawakuchi et al., 2011; Klasen et al., 2016) than to lack of signal resetting. Future work requires
522 targeting of natural subglacial sediments in regions that have quartz with good luminescence
523 characteristics to establish whether robust chronologies from these depositional contexts are indeed
524 possible. A resetting mechanism associated with active transport at the ice-bed interface may also
525 offer potential as a glaciological process tracer. For example, the degree of resetting could be used
526 to quantify sediment strain history or sediment residence times in contemporary systems (Swift et
527 al., 2011).

528

529 **5. Conclusions**

530

- 531 • The occurrence of a small number of zero-dose grains in the shearing zone that increase in
532 number with shearing confirms the preliminary findings of Bateman et al. (2012). Grains
533 either appeared to retain their given dose or had a zero-dose.
- 534 • Data show that grain fracturing or loss of surface material is not responsible for OSL
535 zeroing.

- 536 • Stress variations increased towards the end of the experiments with rapid changes in the
537 order of 18 kPa within a few centimeters of shearing that are interpreted as the build up and
538 collapse of grain bridges. The observed changes in grain characteristics are thought to have
539 led to more bridging with increasing shear distance.
- 540 • Localised high pressure grain-to-grain stresses within bridges (or during their collapse)
541 appear to explain why some grains become zeroed whilst other retain their palaeodose.
- 542 • Relatively short shearing distances might be sufficient to reset a small proportion of the
543 luminescence signal within subglacial sediments. This opens up the potential for future
544 work to successfully apply luminescence dating to sediments contained within subglacial
545 landforms.

546

547 **Acknowledgements**

548 This work followed up the ideas and work of DAS (Swift et al., 2011) and was funded through a
549 Danish Agency for Science Technology and Innovation (FNU) grant 272-08-0492 based on an
550 original application by DAS and held by JAP. Field sampling was undertaken by DAS, MDB and
551 JAP. Ring-shear experiments were carried out by JAP; sediment characterization by DAS, JAP,
552 and AD; with OSL measurements carried out by MDB. Rob Ashurst and Adam Dunajko are
553 thanked for their assistance in sample preparation and sediment characterization. Andrew Murray
554 (Aarhus University) is thanked for enabling the gamma-irradiation to take place at Risø. David
555 Sanderson (Scottish Universities Environmental Research Centre, East Kilbride, Scotland) is
556 thanked for his generous input and guidance at the initial stages of this research. Peter Chung is
557 thanked for providing access to the SEM facility at the Department of Geographical and Earth

558 Sciences, University of Glasgow. Finally, we would like to thank the anonymous reviewer and the
559 journal editor, whose detailed comments and thoughts have helped improve the final manuscript.
560

561

562

563 **References**

- 564 Aitken, M.J., 1985. Thermoluminescence dating. Academic Press, London. 351 pp.
565 Anjar, J., Larsen, N.K., Håkansson, L., Möller, P., Linge, H., Fabel, D., Xu, S., 2014. A ¹⁰Be-
566 based reconstruction of the last deglaciation in southern Sweden. *Boreas* 43, 132-148.
567 Ballantyne, C.K., 2010. Extent and deglacial chronology of the last British-Irish Ice Sheet:
568 Implications of exposure dating using cosmogenic isotopes. *Journal of Quaternary Science* 25,
569 515-534.
570 Ballarini, M., Wallinga, J., Duller, G.A.T., Brouwer, J.C., Bos, A.J.J., Van Eijk, C.W.E., 2005.
571 Optimizing detection filters for single-grain optical dating of quartz. *Radiation Measurements*
572 40, 5 – 12.
573 Bateman, M.D., Catt, J.A., 1996. An absolute chronology for the raised beach deposits at
574 Sewerby, E. Yorkshire, UK. *Journal of Quaternary Science* 11, 389-395.
575 Bateman, M.D., Frederick, C.D., Jaiswal, M.K., Singhvi, A.K. 2003. Investigations into the
576 potential effects of pedoturbation on luminescence dating. *Quaternary Science Reviews* 22,
577 1169–1176.
578 Bateman, M.D., Boulter, C.H., Carr, A.S., Frederick, C.D., Peter, D., Wilder, M. 2007. Detecting
579 post-depositional sediment disturbance in sandy deposits using optical luminescence.
580 *Quaternary Geochronology* 2, 57–64.
581 Bateman, M.D., Carr, A.S., Dunajko, A.C., Holmes, P.J., Roberts, D.L., McLaren, S.J., Bryant,
582 R.G., Marker, M.E., Murray-Wallace, C.V., 2011. The evolution of coastal barrier systems: a
583 case study of the Middle-Late Pleistocene Wilderness barriers, South Africa. *Quaternary*
584 *Science Reviews* 30, 63-81.
585 Bateman, M.D., Swift, D.A., Piotrowski, J.A., Sanderson, D.C.W., 2012. Investigating the effects
586 of glacial shearing of sediment on luminescence. *Quaternary Geochronology* 10, 230-236.
587 Bateman, M.D., Evans, D.J.A., Roberts, D.H., Medialdea, A., Ely, E., Clark C.D. (2018). The
588 timing and consequences of the blockage of the Humber Gap by the last British-Irish Ice Sheet.
589 *Boreas* 47, 41-61.
590 Biegel, R.L., Sammis, C.G., Dieterich, J.M., 1989. The friction properties of a simulated gouge
591 having a fractal distribution. *Journal of Structural Geology* 11, 827–846.
592 Bisschop, J., den Broka, B., Miletich, R., 2005. Brittle deformation of quartz in a diamond anvil
593 cell. *Journal of Structural Geology* 27, 943–947.
594 Boulton, G.S., 1974. Processes and patterns of glacial erosion. In Coates, D.R. (Ed.) *Glacial*
595 *Geomorphology* (Proceedings of the Fifth Annual Geomorphology Symposia, Binghampton),
596 41–87. Allen & Unwin, London.
597 Briant, R.M., Bateman, M.D., 2009. Luminescence dating indicates radiocarbon age
598 underestimation in Late Pleistocene fluvial deposits from eastern England. *Journal of*
599 *Quaternary Science* 24, 916-927.
600 Clark, C.D., Hughes, A.L.C., Greenwood, S.L., Jordan, C., Sejrup, H.S., 2012. Pattern and timing
601 of retreat of the last British-Irish Ice Sheet. *Quaternary Science Reviews* 44, 112-146.
602 Clemmensen, L.B., Murray, A.J., Heinemeier, J., de Jong, R., 2009. The evolution of Holocene
603 coastal dunefields, Jutland, Denmark: A record of climate change over the past 5000 years.
604 *Geomorphology* 105, 303–313.

605 Cohen, D., Iverson, N.R., Hooyer, T.S., Fischer, U.H., Jackson, M., Moore, P.L., 2005. Debris-bed
606 friction of hard-bedded Glaciers. *Journal of Geophysical Research*, 110, F02007.

607 Crawford, E., Mortensen, J.K., 2009. An ImageJ plugin for the rapid morphological
608 characterization of separated particles and an initial application to placer gold analysis.
609 *Computers & Geosciences* 35, 347-359.

610 Damsgaard, A., Egholm, D., Piotrowski, J.A., Tulaczyk, S., Larsen, N.K., Tylmann, K., 2013.
611 Discrete element modeling of subglacial sediment deformation. *Journal of Geophysical*
612 ~~613~~ *Research – Earth Surface* 118, 1-13.

614 Davis, P.T., Bierman, P.R., Corbett, L.B., Finkel, R., 2015. Cosmogenic exposure age evidence for
615 rapid Laurentide deglaciation of the Katahdin area, west-central Maine, USA, 16 to 15ka.
Quaternary Science Reviews 116, 95-105.

616 Dreimanis, A., Hutt, G., Raukas, A., Whippey, P.W., 1978. Dating methods of Pleistocene deposits
617 and their problems: I. Thermoluminescence dating, *Geoscience Canada* 5, 55-60.

618 Drescher, A., de Josselin de Jong, G., 1972. Photoelastic verification of a mechanical model for the
619 flow of a granular material. *Journal of the Mechanics and Physics of Solids* 20, 337–351.

620 Duller, G.A.T., Wintle, A.G., Hall, A.M., 1995. Luminescence dating and its application to key
621 pre-late Devensian sites in Scotland. *Quaternary Science Reviews* 14, 495-519.

622 Duller, G.A.T., Bøtter-Jensen, L., Kohsiek, P., Murray, A.S., 1999. A high-sensitivity optically
623 stimulated luminescence scanning system for measurement of single sand-sized grains.
624 *Radiation Protection Dosimetry* 84, 325–330.

625 Dyke, A.S., Andrews, J.T., Clark, P.U., England, J.H., Miller, G.H., Shaw, J., Veillette, J.J., 2001.
626 The Laurentide and Innuitian ice sheets during the Last Glacial Maximum. *Quaternary Science*
627 *Reviews* 21, 9-31.

628 Evans, D.J.A., Bateman, M.D., Roberts, D.H., Medialdea, A., Hayes, L., Clark, C.D. 2017: Glacial
629 Lake Pickering: stratigraphy and chronology of a proglacial lake dammed by the North Sea
630 Lobe of the British-Irish Ice Sheet. *Journal of Quaternary Science* 32, 295-310.

631 Fuchs, M., Owen, L.A., 2008. Luminescence dating of glacial and associated sediments: review,
632 recommendations and future directions. *Boreas* 37, 636-659.

633 Fukuchi, T., 1989. Increase of radiation sensitivity of ESR centres by faulting and criteria of fault
634 dates. *Earth and Planetary Science Letters* 94, 109–122.

635 Galbraith, R.F., Green, P.F., 1990. Estimating the component ages in a finite mixture. *Radiation*
636 *Measurements* 17, 197-206.

637 Galbraith, R.F., Roberts, R.G., Laslett, G.M., Yoshida, H., Olley, J.M., 1999. Optical dating of
638 single and multiple grains of quartz from Jinmium rock shelter, northern Australia. Part I,
639 experimental design and statistical models. *Archaeometry* 41, 339–364.

640 Gibbard, P.L., Pasanen, A.H., West, R.G., Lunkka, J.P., Boreham, S., Cohen, K.M., Rolfe, C.,
641 2009. Late Middle Pleistocene glaciation in East Anglia, England. *Boreas* 38, 504-528.

642 Godfrey-Smith, D.I., Huntley, D.J. and Chen, W.H., 1988. Optical dating studies of quartz and
643 feldspar sediment extracts. *Quaternary Science Reviews* 7, 373-380.

644 Gueydan, F., Mehl, C., Parra, T., 2005. Stress-strain rate history of a midcrustal shear zone and the
645 onset of brittle deformation inferred from quartz recrystallized grain size. In Gapais, D., Brun,
646 J.P. and Cobbold P.R. (Eds.), Geological Society, London, Special Publications 243, 127-142.

647 Hamblin, R.J.O., Moorlock, B.S.P., Rose, J., Lee, J.R., Riding, J.B., Booth, S.J., Pawley, S.M.,
648 2005. Revised Pre-Devensian glacial stratigraphy in Norfolk, England, based on mapping and
649 till provenance. *Geologie en Mijnbouw* 84, 77-85.

650 Hooke, R.L.B., Iverson, N.R., 1995. Grain-size distribution in deforming subglacial tills: role of
651 grain fracture. *Geology* 23, 57–60.

- 652 Hooyer, T.S., Iverson, N.R., Lacroix, F., Thomason, J.F., 2008. Magnetic fabric of sheared till: A
653 strain indicator for evaluating the bed-deformation model of glacier flow. *Journal of Geophysical*
654 *Research* 113, F02002.
- 655 Houmark-Nielsen, M., 2009. Testing OSL failures against a regional Weichselian glaciation
656 chronology from southern Scandinavia. *Boreas* 37, 660–677.
- 657 Hughes, A.L.C., Gyllencreutz, R., Lohne, O.S., Mangerud, J., Svendsen, J.I., 2016. The last
658 Eurasian ice sheets - a chronological database and time-slice reconstruction, DATED-1. *Boreas*
659 45, 1-45.
- 660 Iverson, N.R., Hooyer, T.S., Hooke, R.L., 1996. A laboratory study of sediment deformation:
661 stress heterogeneity and grain size evolution. *Annals of Glaciology* 22, 167–175.
- 662 Jenson, J.W., Clark, P.U., MacAyeal, D.R., Ho, C., Vela, J.C., 1995. Numerical modelling of
663 advective transport of saturated deforming sediment beneath the Lake Michigan Lobe,
664 Laurentide Ice Sheet. *Geomorphology*, 14, 157-166.
- 665 King, G.E., Robinson R.A.J., Finch, A.A., 2014a. Towards successful OSL sampling strategies in
666 glacial environments: deciphering the influence of depositional processes on bleaching of
667 modern glacial sediments from Jostedal, Southern Norway. *Quaternary Science Reviews* 89,
668 94-107.
- 669 King, G.E., Sanderson, D.C.W., Robinson R.A.J., Finch, A.A., 2014b. Understanding processes of
670 sediment bleaching in glacial settings using a portable OSL reader. *Boreas* 43, 955-972.
- 671 Klasen, N., Fiebig, M., Preusser, F., 2016. Applying luminescence methodology to key sites of
672 Alpine glaciations in Southern Germany. *Quaternary International* 28, 249-258.
- 673 Krumbein, W.C. 1941. Measurement and geological significance of shape and roundness of
674 sedimentary particles. *Journal of Sedimentary Petrology* 11, 64–72.
- 675 Lamothe, M., 1988. Dating till using thermoluminescence. *Quaternary Science Reviews* 7, 273-
676 276.
- 677 Larsen, N.K., Piotrowski, J.A., Christiansen, F., 2006. Microstructures and microscales as proxy
678 for strain in subglacial diamicts: Implications for basal till formation. *Geology* 34, 889-892.
- 679 Larsen, N.K., Piotrowski, J.A., Menzies, J., 2007. Microstructural evidence of low-strain, time-
680 transgressive subglacial deformation. *Journal of Quaternary Science* 22, 593–608.
- 681 Lee, H.K., Schwarcz, H.P., 1994. Criteria for complete zeroing of ESR signals during faulting of
682 the San Gabriel fault zone, southern California. *Tectonophysics* 235, 317–337.
- 683 Lee, J.R., Rose, J., Hamblin, R.J.O., Moorlock, B.S.P., Riding, J.B., Phillips, E., Barendregt, R.W.,
684 Candy, I., 2011. The glacial history of the British Isles during the Early and Middle
685 Pleistocene: Implications for the long-term development of the British ice sheet. *Developments*
686 *in Quaternary Science* 15, 59-74.
- 687 Livingstone S.J., Roberts, D.H., Davies, B.J., Evans, D.J.A., O’Cofaigh, C., Gheorghiu, D.M.,
688 2015a. Late Devensian deglaciation of the Tyne Gap Palaeo-Ice Stream, northern England.
689 *Journal of Quaternary Science* 30, 790-804.
- 690 Livingstone, S.J., Piotrowski, J.A., Bateman, M.D., Ely, J.C., Clark, C.D., 2015b. Discriminating
691 between subglacial and proglacial lake sediments: an example from the Dänischer Wohld
692 Peninsula, northern Germany. *Quaternary Science Reviews* 112, 86-108.
- 693 Li, Y.R., Aydin, A., 2010. Behavior of rounded granular materials in direct shear: mechanisms and
694 quantification of fluctuations. *Engineering Geology* 115, 96–104.
- 695 Mandl, G., de Jong, L.N.J., Maltha, A., 1977. Shear zones in granular material. *Rock Mechanics* 9,
696 95–144.
- 697 Mark, D.M., 1973. Analysis of axial orientation data, including till fabrics. *Geological Society of*
698 *America Bulletin* 84, 1369– 1374.

- 699 McCormack, D.C., Brocklehurst, S.H., Irving, D.H., Fabel, D., 2011. Cosmogenic ^{10}Be insights into
700 the extent and chronology of the last deglaciation in Wester Ross, northwest Scotland. *Journal of*
701 *Quaternary Science* 26, 97-108.
- 702 Menzies, J., Gao, C., Kodors, C. 2013. Microstructural analyses of a Middle Pliocene till from the
703 James Bay Lowlands, Canada—evidence of “potential” fast ice streaming. *Proceedings of the*
704 *Geologists’ Association* 124, 790–801.
- 705 Morozov, G.V. 1968. The relative dating of Quaternary Ukrainian sediments by the TL method.
706 In: VIIIth International Quaternary Association Congress, Paris, USGS Library Catalog No.
707 208 M8208, Washington, p.167.
- 708 Murray, A.S., Clemmensen, L.B., 2001. Luminescence dating of Holocene aeolian sand
709 movement, Thy, Denmark. *Quaternary Science Reviews* 20, 751-754.
- 710 Murray, A.S., Wintle, A.G., 2003. The single aliquot regenerative dose protocol: potential for
711 improvements in reliability. *Radiation Measurements* 37, 377–381.
- 712 Narloch, W., Piotrowski, J.A., Wysota, W., Larsen, N.K., Menzies, J., 2012. The signature of
713 strain magnitude in tills associated with the Vistula Ice Stream of the Scandinavian Ice Sheet,
714 central Poland. *Quaternary Science Reviews* 57, 105-120.
- 715 Narloch, W., Piotrowski, J.A., Wysota, W., Tylmann, K., 2015. Till formation under a soft-bedded
716 palaeo-ice stream of the Scandinavian Ice Sheet, constrained using qualitative and quantitative
717 microstructural analyses. *Sedimentary Geology* 326, 64-78.
- 718 Paterson, W.S.B., 1994. *The Physics of Glaciers*. Butterworth & Heinemann, Oxford.
- 719 Pawley, S.M., Bailey, R.M., Rose, J., Moorlock, B.S.P., Hamblin, R.J.O., Booth, S.J., Lee, J.R.,
720 2008. Age limits on Middle Pleistocene glacial sediments from OSL dating, north Norfolk,
721 UK. *Quaternary Science Reviews* 27, 1363-1377.
- 722 Powers, M.C., 1953. A new roundness scale for sedimentary particles: *Journal of Sedimentary*
723 *Petrology* 23, 117–119.
- 724 Preusser, F., Blei, A., Graf, H.R., Schlüchter, C., 2007. Luminescence dating of Würmian
725 (Weichselian) proglacial sediments from Switzerland: Methodological aspects and
726 stratigraphical conclusions. *Boreas* 36, 130–142.
- 727 Rhodes, E.J., 2000. Observations of thermal transfer OSL signals in glacial quartz. *Radiation*
728 *Measurements* 32, 595–602.
- 729 Rhodes, E.J., Bailey, R.M., 1997. Thermal transfer effects observed in the luminescence of quartz
730 from recent glaciofluvial sediments. *Quaternary Science Reviews* 16, 291–298.
- 731 Rhodes, E.J., Pownall, L., 1994. Zeroing of the OSL signal in quartz from young glaciofluvial
732 sediments. *Radiation Measurements* 23, 581–585.
- 733 Rittenour, T.M., Riggs, N.R., Kennedy, L.E., 2012. Application of single-grain OSL to date quartz
734 xenocrysts within a basalt flow, San Francisco volcanic field, northern Arizona, USA.
735 *Quaternary Geochronology* 10, 300-307.
- 736 Rodnight, 2008. How many equivalent dose values are needed to obtain a reproducible
737 distribution? *Ancient TL* 26, 3-9.
- 738 Sawakuchi, A.O., Blair, M.W., DeWitt, R., Faleiros, F.M., Hyppolito, T., Guedes, C.C.F., 2011.
739 Thermal history versus sedimentary history: OSL sensitivity of quartz grains extracted from
740 rocks and sediments. *Quaternary Geochronology* 6, 261-272.
- 741 Smedley, R.K., Scourse, J.D., Small, D., Hiemstra, J.F., Duller, G.A.T., Bateman, M.D., Burke,
742 M.J., Chiverrell, R.C., Clark, C.D., Davies, S.M., Fabel, D., Gheorghiu, D.M., McCarroll, D.,
743 Medialdea, A., Xu, S., 2017: New age constraints for the limit of the British-Irish Ice Sheet
744 on the Isles of Scilly. *Journal of Quaternary Science* 32, 48-62.
- 745 Sohbaty, R., Murray, A.S., Jain, M., Buylaert, J.-P., Thomsen, K.J., 2011. Investigating the
746 resetting of osl signals in rock surfaces. *Geochronometria* 38, 249-258.

747 Spencer J.Q.G, Hadizadeh, J, Gratiér, J-P and Doan, M-L., 2012. Dating Deep? Luminescence
748 studies of fault gouge from the San Andreas Fault zone 2.6 km beneath Earth's surface.
749 *Quaternary Geochronology* 10, 280-284.

750 Swift, D.A., Sanderson, D.C.W., Nienow, P.W., Bingham, R.B., Cochrane, I.C., 2011. Anomalous
751 luminescence of subglacial sediment at Haut Glacier d'Arolla, Switzerland – a consequence of
752 resetting at the glacier bed, *Boreas* 40, 446-458.

753 Takeuchi, A., Nagahama, H., Hashimoto T., 2006. Surface resetting of thermoluminescence in
754 milled quartz grains. *Radiation Measurements* 41, 826 – 830.

755 Thrasher, I.M., Mauz, B., Chiverrell, R.C., Lang, A. and Thomas, G.S.P., 2009. Testing an
756 approach to OSL dating of Late Devensian glaciofluvial sediments of the British Isles. *Journal*
757 *of Quaternary Science* 24, 785-801.

758 Toucanne, S., Soulet, G., Freslon, N., Silva Jacinto, R., Dennielou, B., Zaragosi, S., Eynaud, F.,
759 Bourillet, J.-F., Bayon, G., 2015. Millennial-scale fluctuations of the European Ice Sheet at the
760 end of the last glacial, and their potential impact on global climate. *Quaternary Science*
761 *Reviews* 123, 113-133.

762 Toyoda, S., Rink, W.J., Schwarcz, H.P., Rees-Jones, J., 2000. Crushing effects on TL and OSL on
763 quartz: Relevance to fault dating. *Radiation Measurements* 32, 667–672.

764 White, T.S., Bridgland, D.R., Westaway, R., Howard, A.J., White, M.J., 2010. Evidence from the
765 Trent terrace archive, Lincolnshire, UK, for lowland glaciation of Britain during the Middle
766 and Late Pleistocene. *Proceedings of the Geologists' Association* 121, 141-153.

767 White, T.S., Bridgland, D.R., Westaway, R., Straw, A., 2016. Evidence for late Middle
768 Pleistocene glaciation of the British margin of the southern North Sea. *Journal of Quaternary*
769 *Science* 32, 261-275.

770 Wright, J.S., 1995. Glacial comminution of quartz sand grains and the production of loessic silt: A
771 simulation study. *Quaternary Science Reviews* 14, 669-680.

772 Zöller, L., Blanchard, H., McCammon, C., 2009. Can temperature assisted hydrostatic pressure
773 reset the ambient TL of rocks? – A note on the TL of partially heated country rock from
774 volcanic eruptions. *Ancient TL* 27, 15-22.

775
776
777

778

Figure Captions

779 **Fig. 1.** The ring shear apparatus used for both experiments. (A) Apparatus loaded with sediment at
780 end of the experiments. (B) The empty ring shear chamber showing the ribs on lid (top of picture)
781 and in the base of the trough used to create shear stress.

782 **Fig. 2.** CAM De values from (A) unsheared and (B) sheared samples with distance sheared.
783 Dashed red line shows the initial gamma dose value. Note final point underwent shearing at an
784 extra 50 kPa

785 **Fig. 3.** FMM De component values (those representing more than 10% of data only) from (A)
786 unsheared and (B) sheared samples with distance sheared. Blue/red indicates dominant component
787 and brown other components extracted. Dashed red line shows the initial gamma dose value. Note
788 final point underwent shearing at an extra 50 kPa

789 **Fig. 4.** Zero-dosed grains measured as a proportion of total number of grains accepted. Note final
790 point underwent shearing at an extra 50 kPa.

791 **Fig. 5.** SEM images of particles from subsamples of unsheared material (above) and sheared
792 material (below) (experiment 1). Unsheared material contains some angular and fractured particles,
793 but many fractures do not appear fresh (e.g., top left) or recent fractures are few in number and
794 asperities typically remain well rounded (e.g., top right). Sheared material contains a larger number
795 of particles with an apparently greater fracture incidence and dominantly angular and sharp
796 asperities (bottom images). Nonetheless, a large proportion of particles in all samples do not show
797 any evidence of fracture, indicating that grain-grain stresses during shearing are highly
798 heterogeneous.

799 **Fig. 6.** Evolution of *round* (calculated on area of longest length; see supplementary information for
800 further details) in shearing-zone subsamples from (A) experiment 1 of Bateman et al. (2012) and
801 (B) experiment 2.

802 **Fig. 7.** Evolution of size in sheared subsamples from (A) experiment 1 and (B) experiment 2. Note
803 the offset between experiments 1 and 2 attributed to inadvertent sorting during subsampling for
804 artificial dosing.

805 **Fig. 8.** Vertical distribution of S_1 eigenvalues in the sediment at the end of experiment 1 after a
806 shearing distance of 1280 cm. Note the relatively high eigenvalues in the shearing zone. Also
807 shown is the distribution of main dip angles (MDA) of elongated grains at each depth, whereby a
808 horizontal line is 0° dip and a vertical line is 90° dip.

809 **Fig. 9.** An example of the sheared sediment collected at the end of experiment 1 after a shearing
810 distance of 1280 cm. (A) Thin section of grains. (B) Black and white image analysis from thin
811 section used to quantify grain orientation.

812 **Fig. 10.** Development of shear stresses and sediment compaction during the ring shear experiment 2
813 under normal stress of 100 kPa (0-1280 cm displacement) and 150 kPa (1280-1920 cm
814 displacement). Note the shear stress heterogeneity evident during the entire experiment believed to
815 have contributed to the variations in D_e distribution; v is the shearing velocity.

816

Table 1
OSL single grain data from shearing experiment; results for the sheared and unsheared samples

Labcode	Shearing Distance (cm)	No. Grains Measured	No. Grains Accepted	Central Age Modelling		Finite Mixture Modelling				D _e Distribution Characteristics		
				Mean D _e (Gy)	OD (%)	Dominant Component D _e (Gy)	Prop (%)	Other Component D _e (Gy)	Prop (%)	Zero Grains N (%) ^a	Skew	Sort
Unsheared												
Shfd11227	0	1200	75	37.0 ± 1.5	32	44.6 ± 2.5	62	27.4 ± 2.0	38	0 (0)	1.37	0.31
Shfd11218	10	1200	64	40.0 ± 1.8	35	41.2 ± 1.5	90			0 (0)	4.91	0.23
Shfd11219	20	1100	73	38.8 ± 1.8	37	40.2 ± 1.4	83	23.4 ± 2.6	15	0 (0)	2.84	0.28
Shfd11220	40	1200	64	38.4 ± 1.4	26	36.7 ± 1.2	94			0 (0)	1.41	0.26
Shfd11221	80	1200	79	34.9 ± 1.1	25	36.3 ± 1.3	93			0 (0)	0.24	0.25
Shfd12091	160	400	49	36.1 ± 2.1	37	36.3 ± 1.7	81	19.9 ± 3.3	11	0 (0)	0.88	0.41
Shfd11223	320	900	67	36.1 ± 1.5	31	37.1 ± 1.0	98			0 (0)	0.46	0.25
Shfd11224	640	1000	61	36.9 ± 1.0	17	36.9 ± 1.0	100			0 (0)	0.22	0.19
Shfd12094	1280	900	80	38.2 ± 1.4	31	35.6 ± 1.6	88	66.0 ± 14.8	12	0 (0)	1.29	0.30
Shfd11226	1920	1200	59	36.5 ± 2.0	40	36.8 ± 1.29	92			0 (0)	2.16	0.29
Sheared												
Shfd12087	10	500	63	38.6 ± 1.5	29	40.8 ± 1.7	91			0 (0)	0.25	0.31
Shfd12088	20	600	69	39.5 ± 1.3	25	37.3 ± 1.4	88			0 (0)	0.68	0.27
Shfd12089	40	700	74	40.9 ± 1.3	21	41.5 ± 1.1	98			0 (0)	0.42	0.32
Shfd12090	80	600	59	38.8 ± 1.2	23	40.4 ± 1.1	98			0 (0)	0.93	0.39
Shfd11222	160	1300	71	35.4 ± 1.4	30	39.1 ± 1.7	82	22.4 ± 3.1	18	2 (2.8)	1.06	0.35
Shfd12092	320	600	73	36.8 ± 1.5	32	39.3 ± 1.4	92			1 (1.4)	0.48	0.30
Shfd12093	640	800	80	37.7 ± 1.3	28	39.0 ± 1.2	96			1 (1.3)	0.48	0.28
Shfd11225	1280	1100	66	35.8 ± 1.5	30	37.6 ± 1.2	95			2 (3)	0.39	0.27
Shfd12095	1920	700	80	43.3 ± 1.7	31	49.7 ± 2.62	73	29.4 ± 3.3	27	8 (10)	0.49	0.47

^a Absolute number of zero-dose grains. In parenthesis, percentage of zero-dose grains as a function of total grains that gave D_e values meeting the quality assurance criteria.

Table 2

OSL single grain data from replicated samples from shearing experiment; the given initial gamma dose was 38.1 ± 1.2 Gy

Labcode	No. Grains Measured	No. Grains Accepted	Central Age Modelling		Finite Mixture Modelling			D _e Distribution Characteristics		
			Mean D _e (Gy)	OD (%)	Dominant Component D _e (Gy)	Prop. (%)	Other Component D _e (Gy)	Prop. (%)	Skew	Sort
Shfd12089(1)	700	74	43.6 ± 1.6	27	46.8 ± 2.0	85	28.3 ± 4.30	15	0.42	0.32
Shfd12089 (2)	300	47	40.6 ± 1.5	22					0.59	0.23
Shfd12089 (3)	700	53	40.9 ± 1.3	21	41.5 ± 1.3	98			0.11	0.21
Shfd12090 (1)	600	59	38.9 ± 1.9	33	32.4 ± 2.1	65	54.9 ± 5.8	35	0.93	0.39
Shfd12090 (2)	600	72	38.0 ± 1.3	28	43.6 ± 2.1	69	27.7 ± 2.3	31	0.21	0.28
Shfd12090 (3)	800	69	39.8 ± 1.2	23	40.4 ± 1.1	98			0.45	0.24

Table 3

Shape parameters used to interpret quantitative particle morphology data obtained by ImageJ analysis of Krumbein plots and optical and SEM images of shearing experiment sediment

Parameter	Example Use or Source	Formula	Comment	Krumbein Scale Comparison ^a
<i>Circ</i>	Roussillon et al. (2009)	$\frac{P_s}{2\sqrt{A_s\pi}}$	Compares perimeter of particle with that of 2D disk of same area. Influenced by elongate particles that deviate from spheroid shape.	+ve (\uparrow <i>Circ</i> value)
<i>rP</i>	Roussillon et al. (2009)	$\frac{P_s}{P_e}$	Use of perimeter of ellipse intended to remove influence of particle elongation when attempting to capture roundness.	+ve (\uparrow <i>rP</i> value)
<i>Conv</i>	Roussillon et al. (2009)	$\frac{A_s}{A_{CH}}$	Convex hull fitted to particle (rather than ellipse) further removes influence of elongation when attempting to capture roundness.	-ve (\downarrow <i>Conv</i> value)
<i>Conv2</i>	Cox and Budhu (2008)	$\frac{P_{CH}}{P_s}$	As <i>Conv</i> (above) but uses particle perimeter and convex hull perimeter rather than area.	-ve (\downarrow <i>Conv2</i> value)
<i>Round</i>	Cox and Budhu (2008)	$\frac{4A_s}{\pi L_{\text{Ferret}}^2}$	Relates area to longest length. Sensitive to evolution of 'sharp', elongated forms.	-ve (\downarrow <i>Round</i> value)

^a Regression using reversed Krumbein (1941) scale (Fig. S1). All relationships significant at $p < 0.001$.

Table 4

Shape parameters calculated by the QICPIC analysis software (<https://www.sympatec.com/EN/ImageAnalysis/Fundamentals.html>); for details on terms within the formulas see Table S1

Parameter	Formula	Comment	Interpretation
<i>Sphericity</i>	$\frac{2\sqrt{A_s}\pi}{P_s}$	Circularity in for a 2D shape. Identical to inverse of <i>Circ</i> (Table S1). Influenced by particle elongation.	↑angularity = ↓ <i>Sphericity</i>
<i>Aspect Ratio</i>	$\frac{L_{\min}}{L_{\text{Ferret}}}$	Ratio of shortest to longest axis. Measures particle elongation (similar to ratio of B-axis to A-axis).	↑ angularity = ↓ <i>Aspect Ratio</i>
<i>Convexity</i>	$\frac{A_s}{A_{CH}}$	Identical to <i>Conv</i> (Table S1). Convex hull fitted to particle eliminates influence of elongation.	↑angularity = ↓ <i>Convexity</i>

Table 5
Shape formula variables (Tables 3 and 4)

Variable	Description
P_s	perimeter of the particle silhouette
P_e	perimeter of the smallest ellipse that encloses the particle silhouette
A_s	area enclosed by the particle silhouette
P_{CH}	perimeter of the smallest convex hull that encloses the particle silhouette
A_{CH}	area of the smallest convex hull that encloses the particle silhouette
L_{Ferret}	length of the particle's Feret diameter
L_{min}	length of the particle's shortest axis

Table 6

Trend and statistical significance of changes in particle shape and size during shearing; regression was undertaken on log-transformed shearing distance values for all analyses.

Experiment/Zone	<i>Optical and SEM Image</i>					<i>QICPIC Analysis</i>			<i>Particle diameter analysis</i>	
	<i>Circ</i>	<i>rP</i>	<i>Conv</i>	<i>Conv2</i>	<i>Round</i>	<i>Sphericity</i>	<i>Convexity</i>	<i>Aspect ratio</i>	Surface mean diameter	Volumetric Mean Diameter
Krumbein	↑↑↑	↑↑↑	↓↓↓	↓↓↓	↓↓↓					
Experiment 1/sheared	↑↑↑	↑	↓	↓↓	↓↓		↑↑↑		↑↑↑	↑↑↑
Experiment 2/sheared	↓↓	↑↑↑		↑↑↑		↑↑↑	↑↑↑	↑	↓↓↓	↓↓↓
Experiment 2/unsheared	↑↑		↓↓		↓↓	↑	↑↑↑	↑↑↑	↑	↑

Key: ↑↑↑ $p \leq 0.05$; ↑↑ $p \leq 0.1$; ↑ $p \leq 0.35$; ↑ positive and ↓ negative correlation; x indicates $p > 0.35$.

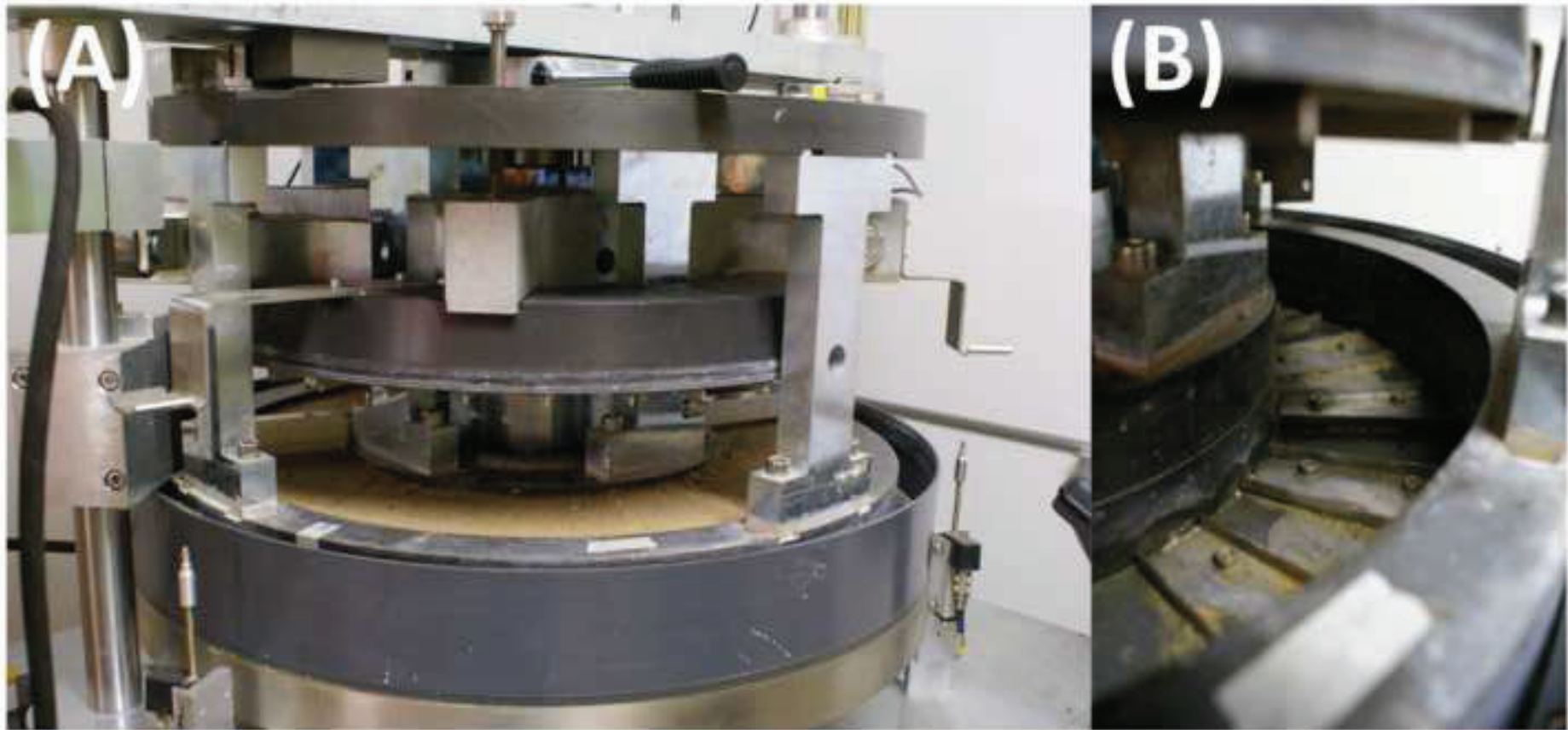
Table 7

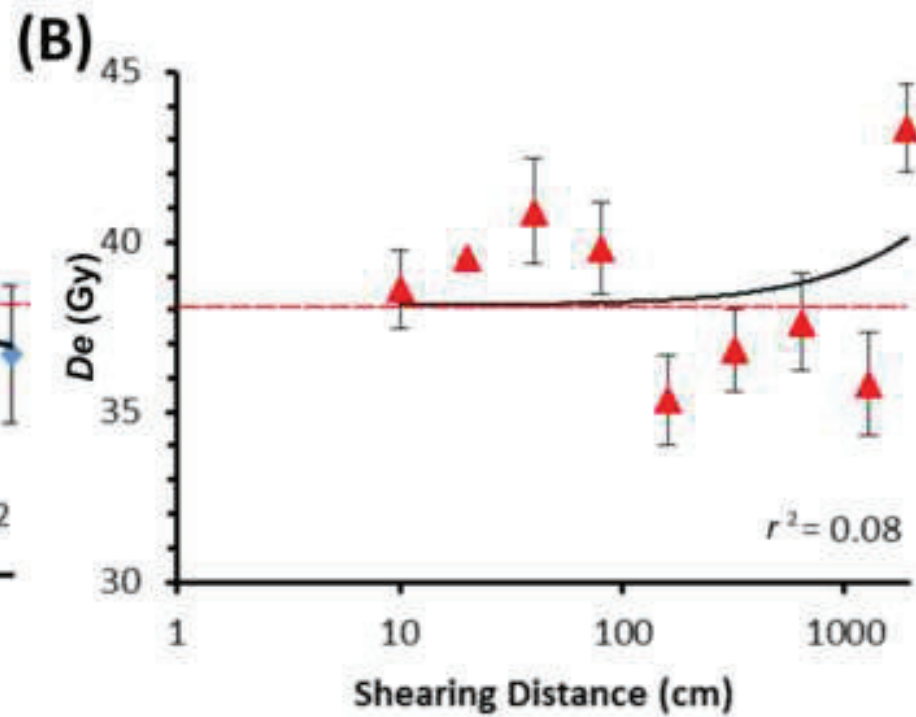
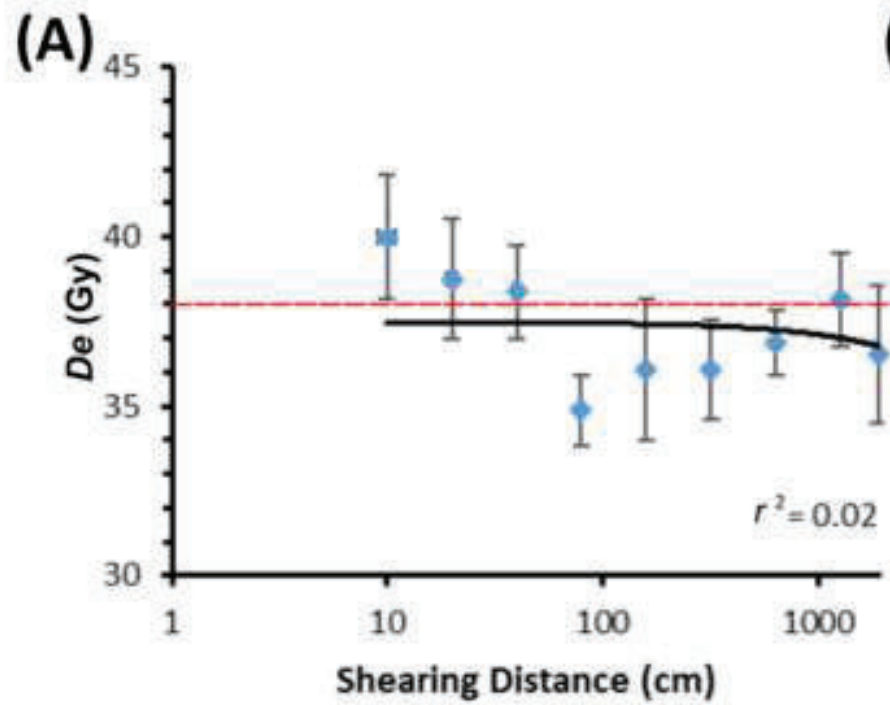
Trend and statistical significance of changes in particle shape quantified using Power's roundness (see text) and fracture incidence analysis; all regressions undertaken on log-transformed shearing distance values

Experiment/zone	<i>R</i>	<i>%Frac</i>	<i>%R</i>	<i>%A</i>	<i>%VA</i>
Experiment 1/sheared	↓↓↓	↑↑↑	↓↓↓	↑↑↑	-
Experiment 2/sheared	↓↓↓	↑↑	↓↓	↑↑↑	↑↑
Experiment 2/unsheared	-	-	-	-	-

Key: ↑↑↑ $p \leq 0.05$; ↑↑ $p \leq 0.1$; ↑ positive and ↓ negative correlation; - indicates $p > 0.1$.

Figure (Color)
[Click here to download high resolution image](#)





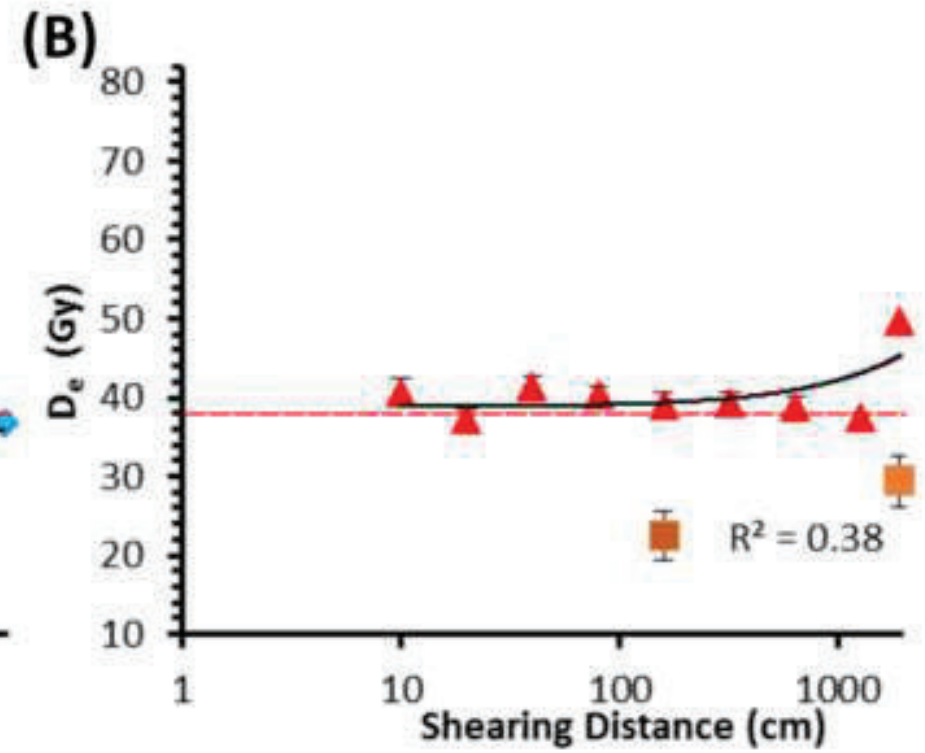
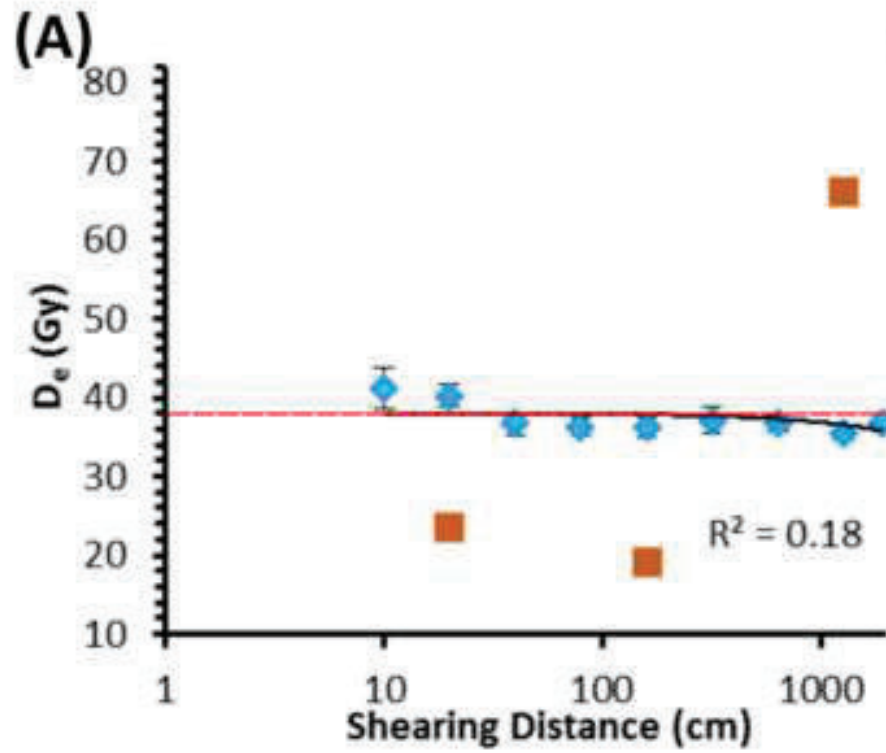
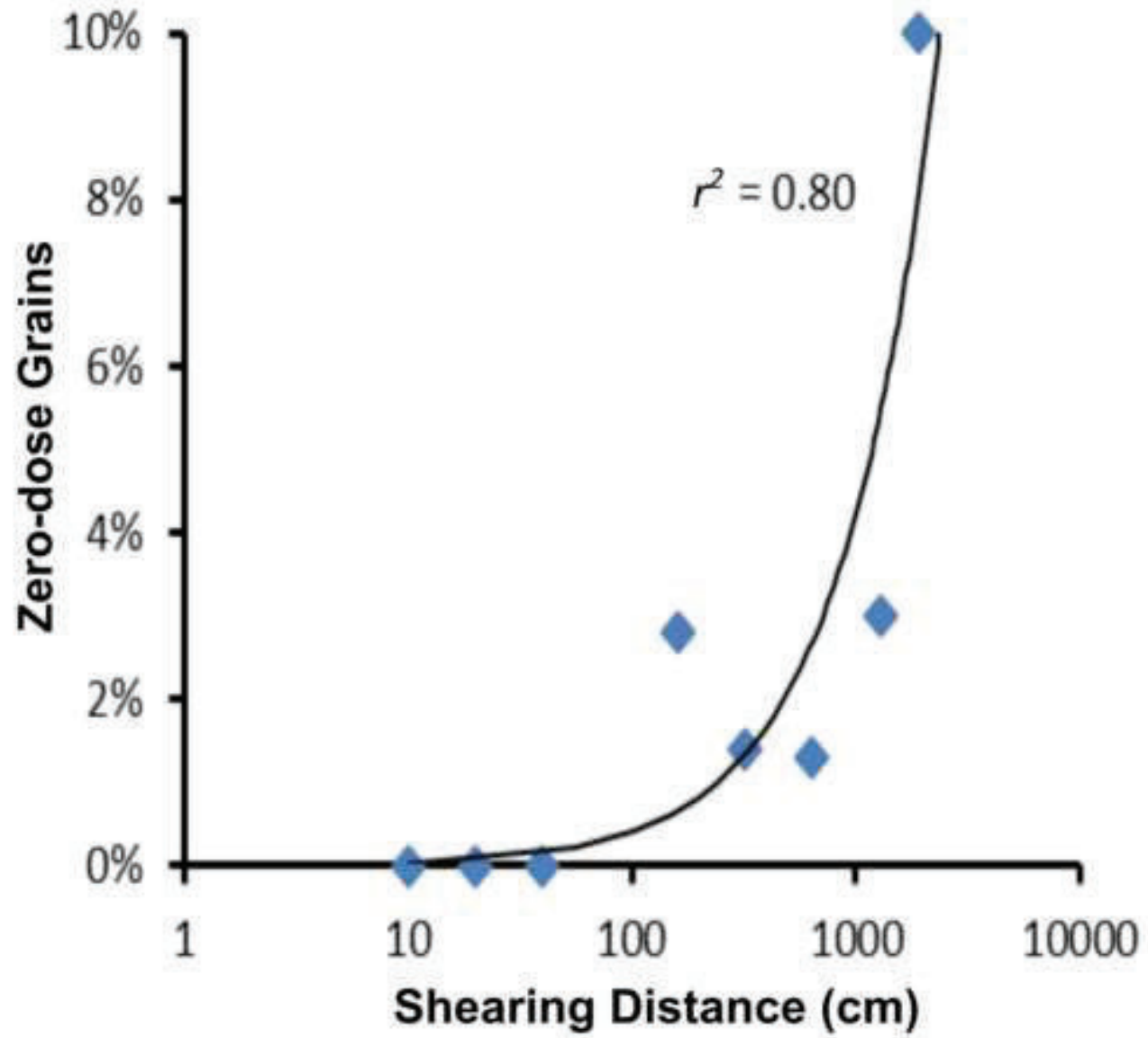
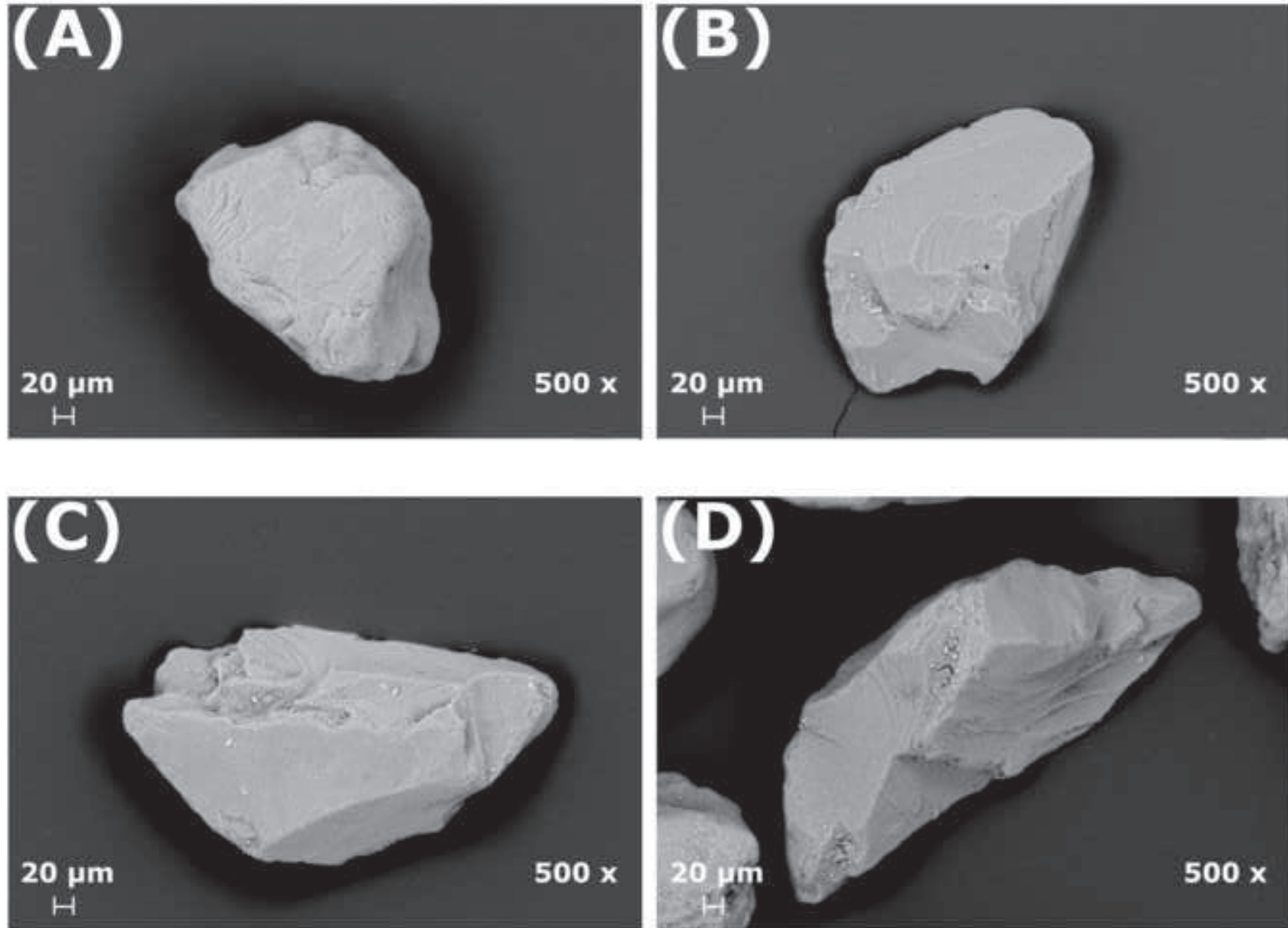
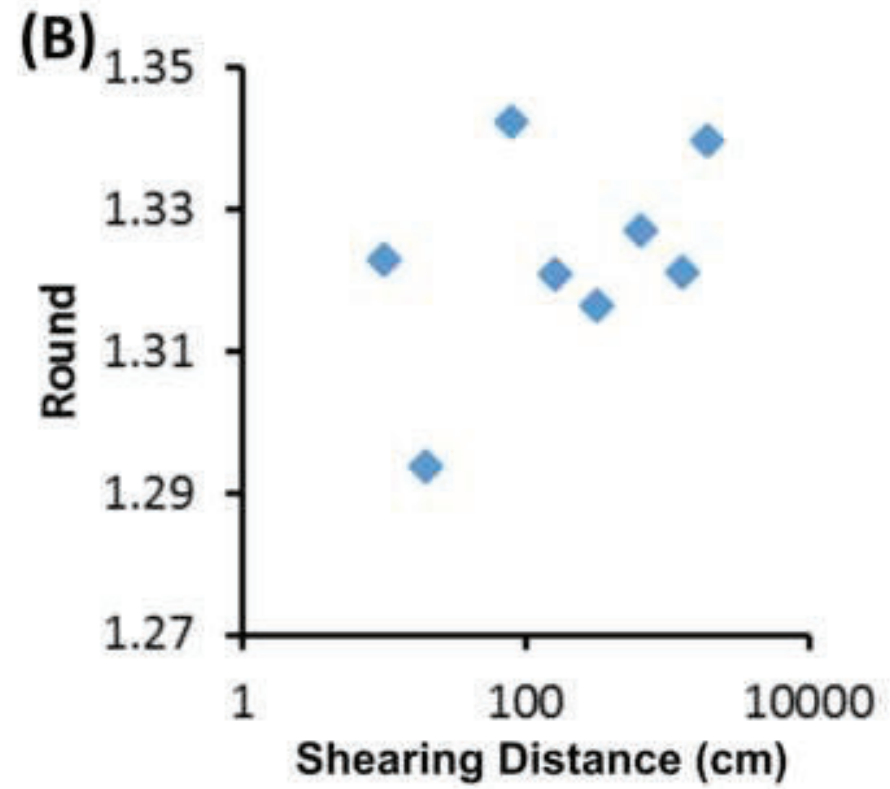
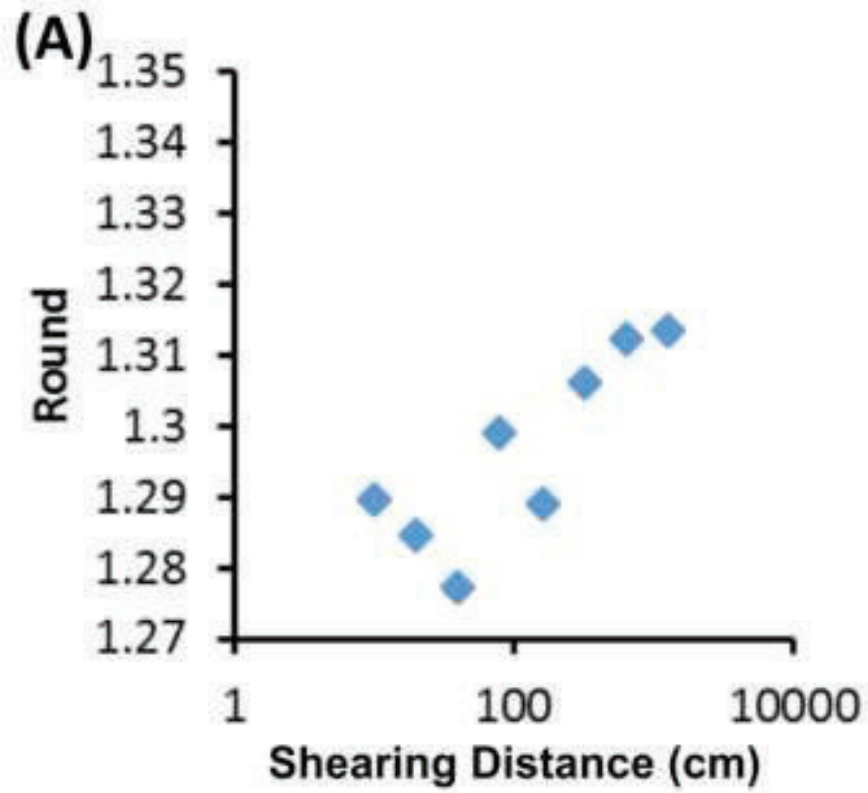


Figure (Color)

[Click here to download high resolution image](#)







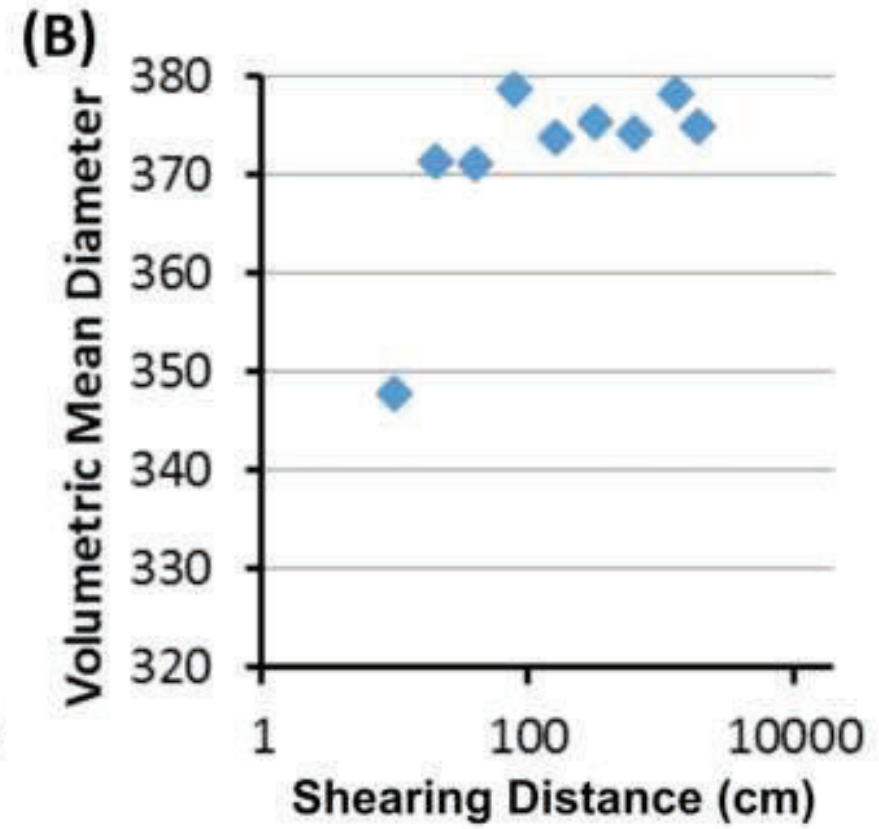
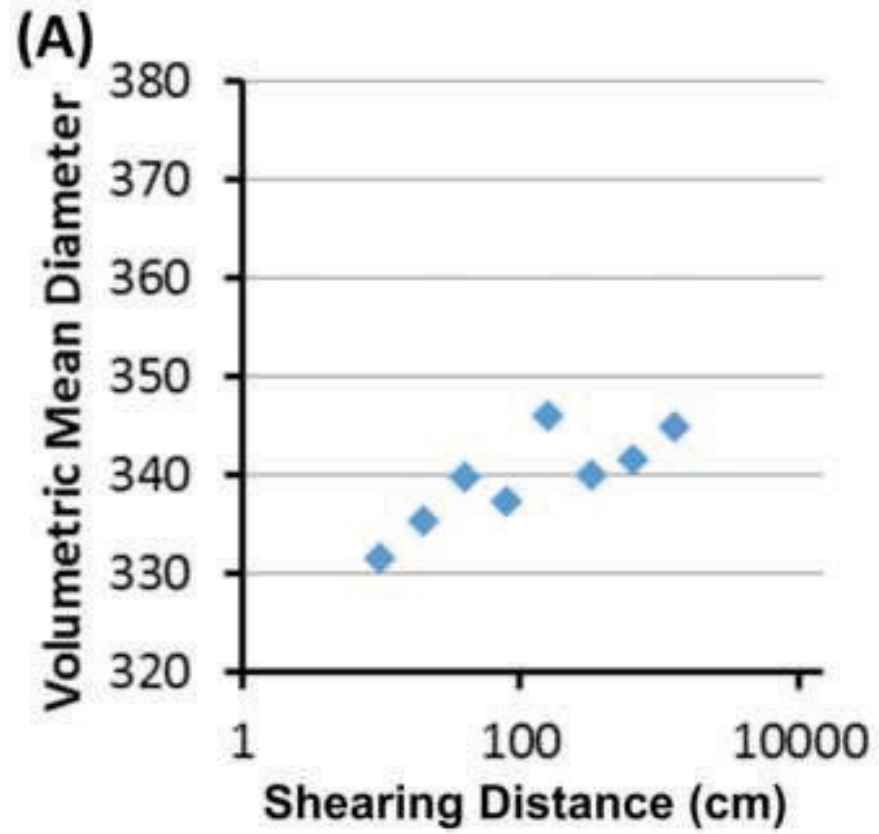
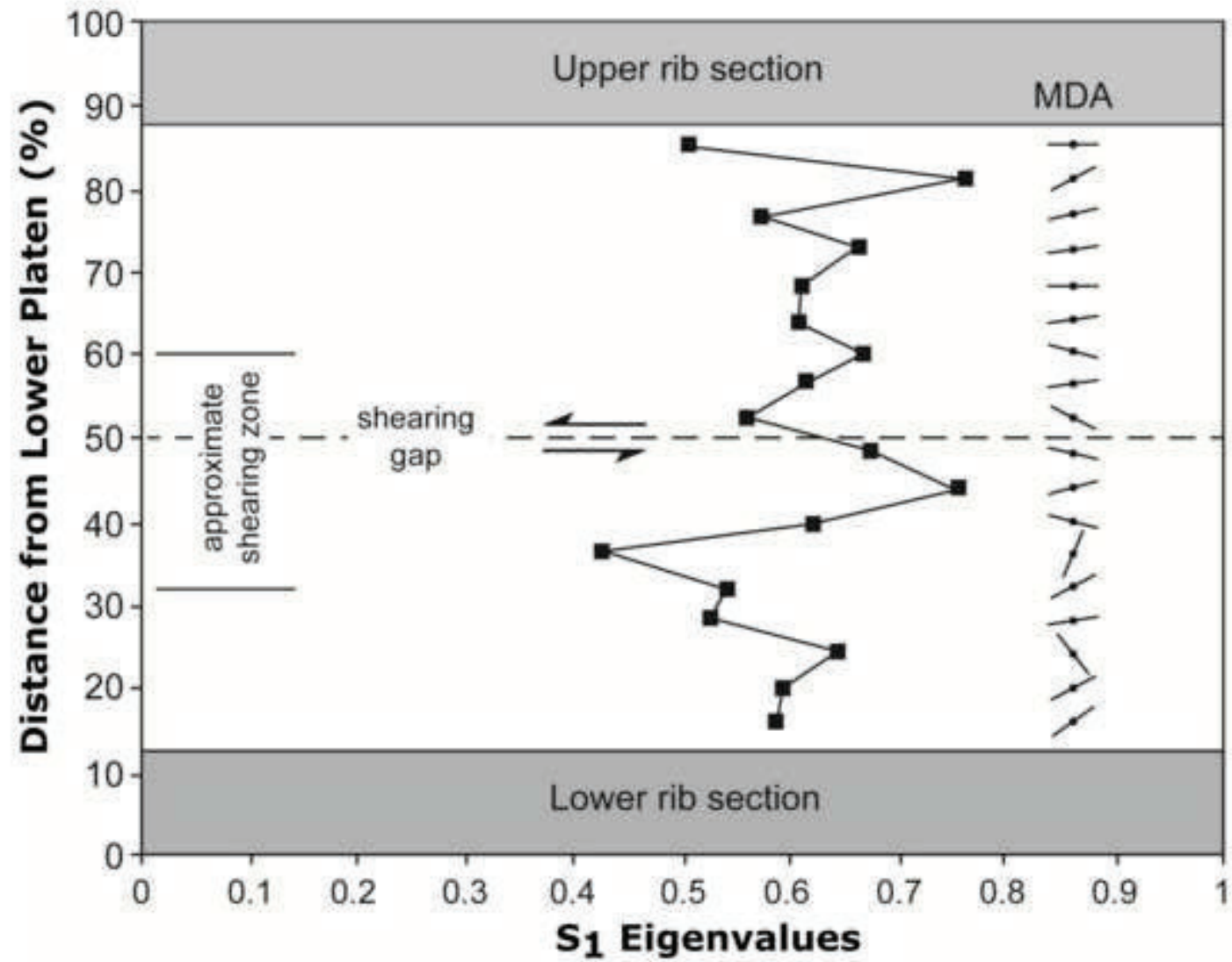


Figure (Color)

[Click here to download high resolution image](#)



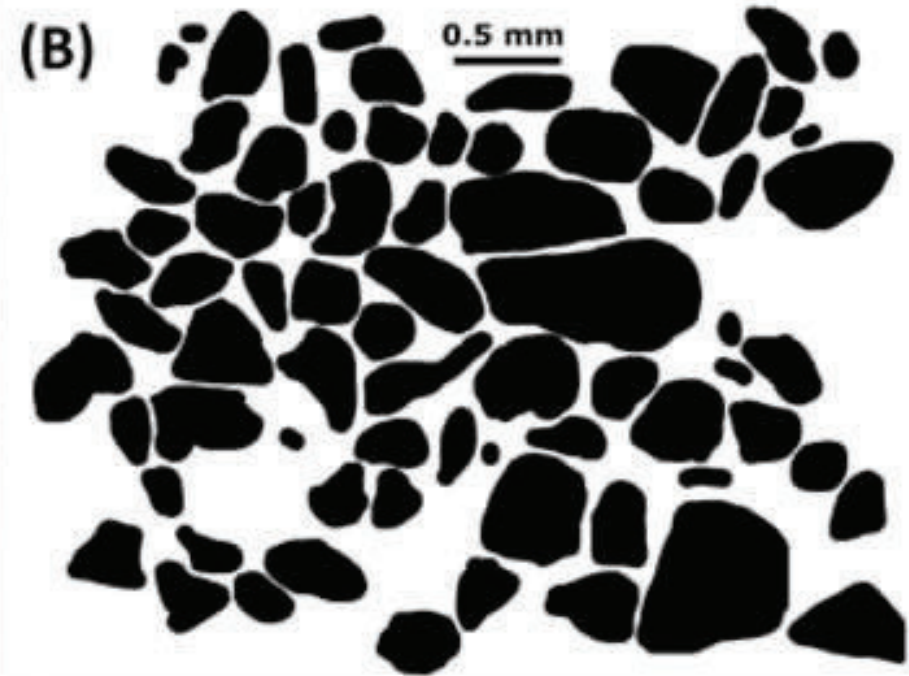
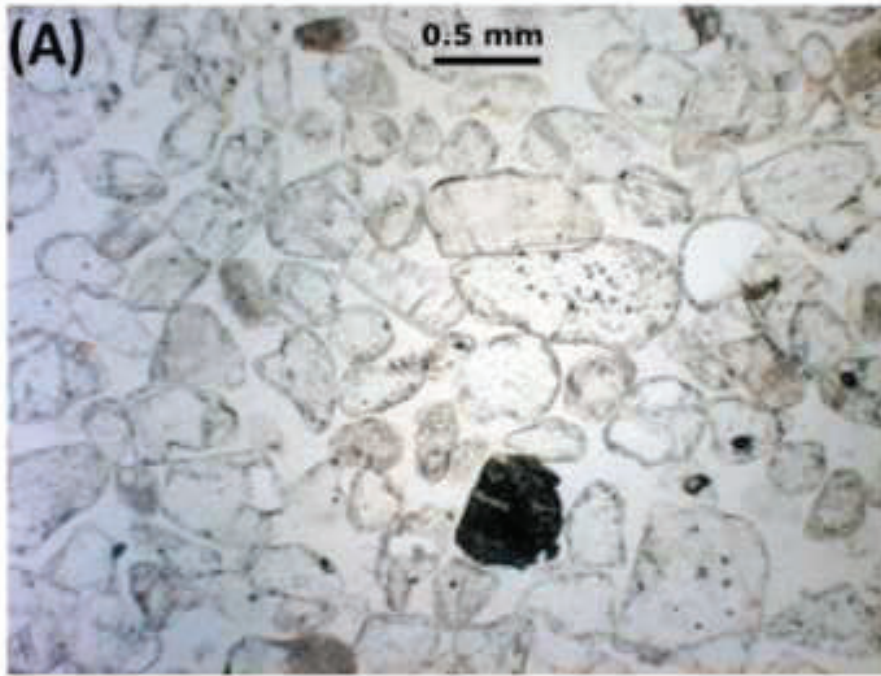


Figure (Color)

[Click here to download high resolution image](#)

